Numerical and Experimental Investigation of Membrane Distillation Flux and Energy Efficiency

by

Jaichander Swaminathan

B. Tech., Indian Institute of Technology Madras (2012)

Submitted to the Department of Mechanical Engineering
in partial fulfillment of the requirements for the degree of

Master of Science in Mechanical Engineering

at the

MASSACHUSETTS INSTITUTE OF TECHNOLOGY

June 2014

Author .....
Department of Mechanical Engineering
May 18, 2014

Certified by .....
John H. Lienhard V
Collins Professor of Mechanical Engineering
Thesis Supervisor

Accepted by .....
David E. Hardt
Chairman, Committee on Graduate Theses

Numerical and Experimental Investigation of Membrane Distillation Flux and Energy Efficiency

by

Jaichander Swaminathan

Submitted to the Department of Mechanical Engineering
on May 18, 2014, in partial fulfillment of the
requirements for the degree of
Master of Science in Mechanical Engineering

Abstract

While the field of desalination has matured for seawater desalination and similar applications, other markets such as the treatment of high salinity feed streams require novel technological innovations. This thesis considers membrane distillation (MD), one of the relatively less studied desalination technologies. The energy efficiency of MD in the sweeping gas (SGMD) configuration along with a multi-tray bubble column dehumidifer is analyzed and compared to other conventional configurations. The single stage SGMD systems studied have relatively low GOR (approximately 2-3) compared to other MD systems. The system mass flow rates and top and bottom temperatures together define optimal operating points of the system. An experimental apparatus designed to analyze scaling and fouling in MD is described in detail along with a discussion of the practical challenges faced and their solutions. Experiments are conducted at various feed temperatures, flow rates and salinities ,and a numerical model of heat and mass transport in MD is validated. MD can treat feed solutions at very high salinities (200 ppt) and still produce extremely pure permeate with salinity less than 0.1 ppt. The experimental apparatus is also used to study the effect of module inclination angle on Air Gap MD flux performance and these results compared with theoretical predictions to determine the optimal orientation of the AGMD apparatus.

Thesis Supervisor: John H. Lienhard V
Title: Collins Professor of Mechanical Engineering

Acknowledgments

I am grateful to my advisor, Prof. John Lienhard for his guidance throughout the course of this project.

I would like to thank Edward Summers for sharing his MD numerical models and his experimental expertise. Thanks David, for being a great co-researcher. Thanks to all my lab-mates for their continuous encouragement and for providing useful feedback.

I would like to thank our collaborators at Masdar University, Prof. Hassan A. Arafat and Dr. Elena Guillen-Burrieza for sharing their insights and helping out along the way.

I would like to acknowledge the contributions of MIT undergraduate students Sarah Ritter, Laith Maswadeh, Aileen Guttman, Joanna K. So and Sterling Watson in the design and building of several components of the experimental setup described in this thesis.

This work was funded by the Cooperative Agreement between the Masdar Institute of Science and Technology (Masdar Institute), Abu Dhabi, UAE and the Massachusetts Institute of Technology (MIT), Cambridge, MA, USA - Reference 02/MI/MI/CP/11/07633/GEN/G/00.

Contents

List of Figures

List of Tables

Nomenclature

Roman symbols		**Units**
B	membrane distillation coefficient	kg/m^2 s Pa
c_p	specific heat at constant pressure	J/kgK
d	channel depth	m
dA	area element	m^2
dz	elemental length	m
h	specific enthalpy	J/kg
h_{fg}	enthalpy of vaporization	J/kg
J	mass flux	kg/m^2 s
k_{mass}	mass transfer coefficient	m/s
L	module effective length	m
$\dot{m}$	mass flow rate	kg/s
$\dot{m}_{\text{r}}$	air water mass flow rate ratio	-
MW	molecular weight	kg/kmol
n_{cells}	number of computational cells	-
P	pressure	Pa
p	partial pressure	Pa
q	heat flux	W/m^2
$\dot{Q}$	rate of heat addition	W
s	specific entropy	J/kg K
S, sal	salinity	g/kg
$\dot{S}_{\text{gen}}$	entropy generation rate	W/K
$\dot{s}_{\text{gen}}$	specific entropy generation	J/kg K
T	temperature	^{o}C
v	velocity	m/s
w	module width	m
x	mole fraction	-
z	distance along module length	m

Greek symbols

α	heat transfer coefficient	W/m^2 K
δ	thickness of membrane	m
δ	film thickness in AGMD	m
ϵ	porosity	%
γ	activity coefficient	
ω	humidity ratio	kg/kg
ρ	density	kg/m^3

Subscripts

$(\cdot)_{a}$	air
$(\cdot)_{b}$	bulk/free stream
$(\cdot)_{c}$	coolant
$(\cdot)_{da}$	dry air
$(\cdot)_{eff}$	effective
$(\cdot)_{f}$	feed
$(\cdot)_{gap}$	air gap
$(\cdot)_{in}$	inlet
$(\cdot)_{m}$	membrane
$(\cdot)_{out}$	outlet
$(\cdot)_{p}$	permeate
$(\cdot)_{sg}$	sweeping gas
$(\cdot)_{v}$	vapor
$(\cdot)_{vap}$	vapor pressure
$(\cdot)_{wb}$	wet bulb
$(\cdot)_{w}$	water

Acronyms

AGMD	Air Gap Membrane Distillation	
BCDH	Bubble Column Dehumidifier	
DCMD	Direct Contact Membrane Distillation	
DBT	Dry Bulb Temperature	°C

EES	Engineering Equation Solver	
GOR	Gained Output Ratio	-
MD	Membrane Distillation	
MSBCDH	Multistage Bubble Column Dehumidifier	
SGMD	Sweeping Gas Membrane Distillation	
VMD	Vacuum Membrane Distillation	
MD	Membrane Distillation	
MED	Multiple Effect Distillation	
MSF	Multiple Stage Flash	
ppt	Parts per thousand	g/kg
ppm	Parts per million	mg/kg
TTD	Terminal Temperature Difference	°C

Chapter 1

Introduction

Desalination technologies are being used today as a source of fresh water in water stressed regions of the world that have access to sea or brackish water. With rapidly growing populations and increasing energy use and standards of living, more regions of the world are getting water stressed [3]. Increased water reuse and improvements in efficiency of water purification and desalination technologies can help tackle these problems.

Significant improvements have been made in desalination technologies since their first appearance. Membrane research for reverse osmosis (RO) has resulted in a sharp reduction in membrane manufacturing costs and an increase in membrane permeability, leading to RO dominating the seawater desalination market at present. More the 60 % of the desalination installations in the world as of 2012 have are RO plants and this fraction is steadily increasing [4] (Fig. 1-1). A study by Mistry et al. [5] showed that in terms of second law efficiency, RO is way ahead of most other technologies with lower relative irreversibilities.

1.1 Need for Alternate Desalination Technologies

In addition to producing pure permeate water, desalination systems also produce a concentrated brine stream. The concentration of this brine stream is a function of the feed water quality and ratio of pure water recovered in the system. In the case of

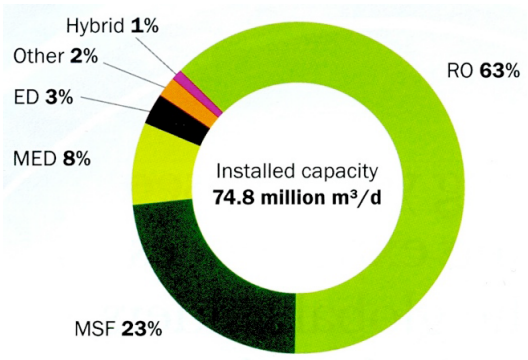

Figure 1-1: Contributions of different technologies to total worldwide installed desalination capacity as of 2012

seawater RO, this brine (which exits at a salinity of about 70 ppt) is almost universally just disposed back in to the ocean at some distance from the shore. In the case of inland desalination systems however, we do not have the convenience of having a sink to deposit this byproduct. Re-injection into the ground can cause ground water to get contaminated, thereby increasing future treatment costs. As a result, in some of these applications, Zero Liquid Discharge (ZLD) is necessary.

Reverse osmosis systems rarely go beyond a brine salinity of 70 ppt at which point a pressure of 60 bar is required to keep pure water flowing from the feed to the permeate side. While it is not completely clear whether it is the strength of the membrane to withstand high pressures or the cost of pressure vessels that limits the process at 69 bar, current systems universally stop at this salinity of the feed. Researchers have noted the need for alternate technologies to treat waters at higher salinities.

While ZLD is one scenario which requires desalination of waters beyond the range of applicability of RO, there are some feed waters that start out at much higher salinities than seawater. The hydraulic fracturing industry that has recently caused a boom in the production of shale gas in the US has high salinity flow-back or produced water as one of its by products. This water can be more than 4-5 times saltier than seawater [6]. Since the number of fracking wells is increasing and the wells are spatially spread out over a large area, the need for scalable desalination technologies that can

handle a wide range of salinities of inlet feed waters has emerged.

While RO produces very pure permeate quality (99.99% rejection) in many cases, some solutes still find their way through the RO membrane. Boron is the most famous example of this; and, since boron is inimical to agriculture, Israel which uses reclaimed wastewater that originates as desalinated water for agriculture has to use multiple passes through RO systems, significantly increasing energy consumption and costs. For certain industrial applications too, the water quality requirements might be more stringent than what RO can guarantee. This is another niche market where other technologies may be required.

1.2 Membrane Distillation for Desalination

Thermal desalination technologies that work on the principle of effecting separation of pure water from a saline solution through phase change are not fundamentally limited by the salinity of the feed solution. As a result, these technologies have been actively investigated as alternatives to RO for high salinity feed streams in the past few years. Some examples of such systems include the older multi-stage flash and multi-effect distillation and the newer humidification dehumidification systems.

Membrane distillation (MD) is a thermal technique for desalination has been receiving increased attention in the academic and research community in recent years [7]. Low system complexity, scalability and ability to use low temperature and waste heat sources, including for example geothermal and solar energy, makes MD an attractive prospect for renewable desalination systems.

Figure 1-2 shows different configurations of MD that have been considered. These include Direct Contact (DCMD), Air Gap (AGMD), Sweeping Gas (SGMD), and Vacuum Membrane Distillation (VMD) based on the conditions on the other permeate side of the membrane.

Of these, while the performance of single stage configurations of AGMD, SGMD and VMD have been analyzed earlier [2], SGMD has not been analyzed from an energy efficiency standpoint. Chapter 1 deals with numerical analysis of energy efficiency of

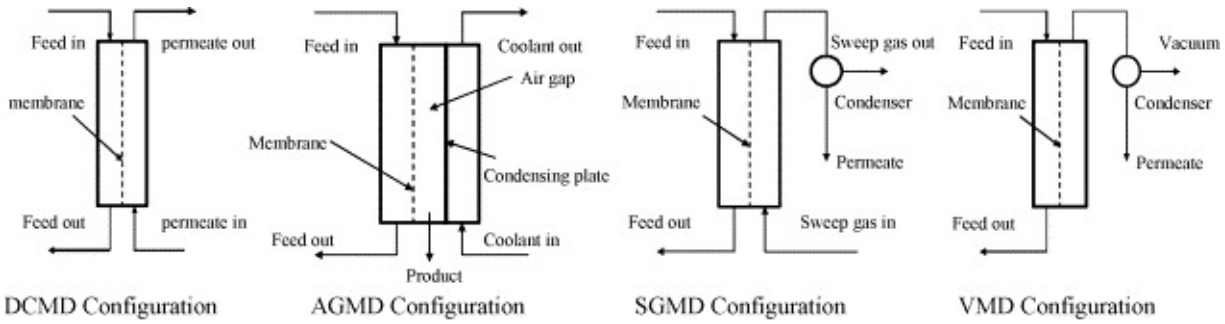

Figure 1-2: Schematic diagram of various membrane distillation systems (from [1])

SGMD to understand its performance in relation to other technologies and identify means of reducing irreversibilities and improving energy efficiency of the system.

Chapter 4 of this thesis deals with the effect of module orientation on performance of AGMD in terms of flux or rate of permeate production. While most AGMD systems have been used in the vertical orientation, the advantages or disadvantages of other module orientations including the horizontal orientation have not been discussed in much detail in the literature. Experimental results are presented and the possibility of water bridging and flooding in the air gap are discussed.

1.3 Fouling in Membrane Distillation

In spite of its advantages, significant advancements are needed in membrane technology for MD to reach cost competitiveness and enable market share growth [8]. Fouling in membrane distillation is of particular importance in this regard, as fouling increases costs of energy consumption, downtime, cleaning, required membrane area, required membrane replacement, and creates problems with product water contamination from pore wetting [9, 10].

While increased research interest in MD is relatively recent [11], scaling under high temperature conditions has been a key problem in systems that use hot water since the advent of the steam engine. Research in the area, especially for metal heat exchanger fouling, originated well before 1900 [12]. These studies are limited to understanding the effect of increased surface heat transfer resistance due to the formation of scale

formation. In the case of MD and other membrane technologies, in addition to its influence on heat transfer resistances, scaling can significantly affect mass transport phenomena leading to lower flux and reducing overall system performance [12]. RO scaling has been extensively investigated and data from real RO systems is available. However, RO membranes are virtually non-porous, are comprised of different materials, and operate at much lower temperatures and much higher pressures than MD. Therefore, RO membranes exhibit significantly different fouling characteristics than MD membranes [13, 9, 12, 14].

Studies focused on scaling in MD largely originated in the 1990s and are becoming more numerous [8, 11]. Between 1991 and 2011, sixteen MD systems were tested at the pilot or semi-pilot scale [15]. Limited fouling data from those plants constitute most of what we know about the fouling potential of MD membranes and the damage they may sustain under actual field operation conditions. For many years, it was believed that the hydrophobic nature of the membrane and the low feed pressure in the MD process are sufficient to prevent the feed solution from penetrating the membrane pores and from causing significant scaling on its surface. For example, in 2003, Koschikowski et al. [16] stated that for MD membranes, "chemical feed water pre-treatment is not necessary; intermittent operation of the module is possible; and contrary to RO, there is no danger of membrane damage if the membrane falls dry". This has been the widely accepted notion about the ability of MD systems to withstand dry out periods and to operate intermittently. In fact, this is how most solar-powered MD plants operated, intermittently (shutting down overnight) and allowing the membranes to fall dry for hours every day [16, 17, 18, 19]. Intermittent operation can also result from unstable solar conditions or an uneven distribution of flux [19]. While it may be true that MD membranes are relatively more resistant to fouling, they remains vulnerable to it and often require well engineered designs and operating conditions to avoid and to mitigate damage or destruction of the membranes by fouling.

Current MD membranes are adapted from micro-filtration and similar markets. Commercial availability of membranes that are specifically designed for MD desali-

nation is scarce [11]. Several researchers are actively working on the development of membranes specially tailored for MD. Understanding the fouling characteristics of MD membranes under various operating conditions and with the use of different feed solutions can help improve novel MD membranes, and design systems to operate under safer conditions.

Chapter 3 describes the construction of an MD experimental setup that can be used to characterize fouling under well defined feed temperature, flow and salinity conditions. Experiments conducted with high salinity sodium chloride feed solutions, as a baseline case to understand the effect of the temperature and concentration boundary layer resistances are also discussed.

Chapter 2

Energy Efficiency of Sweeping Gas Membrane Distillation Systems

Abstract

Sweeping Gas Membrane Distillation (SGMD) is a carrier gas membrane distillation technology that can use low temperature, low grade and waste heat sources and is well suited to small scale desalination systems. Understanding the overall thermal efficiency, usually in the form of a Gained Output Ratio (GOR), is an important step its towards commercial implementation. This chapter presents a 'one dimensional' numerical model of the heat and mass transfer processes in a flat sheet SGMD module coupled to a multi-tray bubble column dehumidifier (MBCD). The model is validated against flux data reported in literature. It is used to analyze entropy generation and study the effect of various parameters on the efficiency of SGMD desalination cycles. While previous studies have focused on the MD segment and on improving flux, entropy generation in both the SGMD module and the dehumidifier can be important and they both affect the overall cycle efficiency. GOR values in excess of 2.5 are observed in single stage once through SGMD-MBCD desalination cycles.

2.1 Introduction

In membrane distillation (MD), desalination is achieved by passing water vapor through the pores of a hydrophobic membrane by establishing a temperature-driven vapor pressure difference between the feed and permeate sides of the module. The hydrophobicity of the membrane ensures that liquid water does not pass through and

thereby ensures almost 100% elimination of non-volatile impurities such as salt in the permeate. Hot saline water constitutes the feed in these systems. Based on the design of the permeate side, MD processes have been classified into four major categories - Direct Contact (DC), Air Gap (AG), Sweeping Gas (SG), and Vacuum (V) MD. [20]

DCMD has a cold pure water stream flowing counter-current to the feed on the permeate side, onto which the vapor condenses immediately after crossing the membrane. Since the hot and cold streams are separated only by a thin membrane, there is significant sensible heat transfer. This heat transfer, in addition to being a loss, also adds to temperature polarization in the streams [21]. AGMD on the other hand has a cold condensing plate separated from the membrane by a thin layer of stagnant air. This way, sensible heat loss from the feed is reduced since air has a lower thermal conductivity. The evaporated water has to diffuse through the air gap and reach the film of condensate on the cold plate which becomes one of the rate limiting steps. SGMD has an air stream that flows on the permeate side picking up the incoming vapor and getting humidified as it moves along the module. Generally the temperature of air also increases along the module. The hot humid air is then cooled in a condenser where product water is recovered. Although SGMD combines advantages of both DCMD (lower mass transfer resistance on the permeate side) and AGMD (lower sensible heat loss across the membrane) configurations, since additional equipment (dehumidifier) is required to condense the product water out of the air stream, it has received scant attention compared to other types of MD technology, both in theoretical and experimental studies [1]. Until 2011, only 4.5% of papers related to MD were on SGMD [11].

With the development of compact, high-effectiveness and low cost dehumidifiers [22], SGMD has the become more competitive as a means to purify water. Most literature on MD has focused on improving membrane flux rather than on energy efficiency (GOR), which is the relevant parameter for comparison with other established thermal desalination technologies such as MSF and MED [2]. Therefore, in this study, we develop a numerical model of the heat and mass transfer processes within a SGMD module, which is then coupled with a dehumidifier model to form a complete

desalination system for efficiency analysis.

2.1.1 SGMD Process

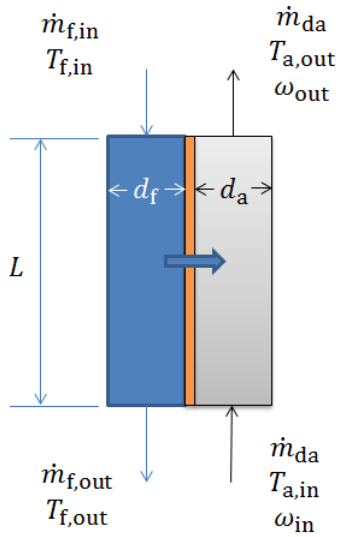

Figure 2-1: Schematic diagram of SGMD process

Figure 2-1 shows a schematic diagram of the SGMD module. The feed stream and the air stream flow counter-current to each other. The feed inlet temperature is of the order of $T_{f,in} \approx 60\,^{\circ}\text{C}$. The air stream generally enters at a lower temperature of about $T_{a,in} \approx 25\,^{\circ}\text{C}$. Both heat and mass are transferred from the hot feed side to the air stream. The temperature and humidity of the air stream increase along the module whereas the feed cools down before exiting.

The driving force for heat transfer is the difference in temperature (dry bulb temperature - DBT, for the air stream) between the stream. Mass transfer is driven by the vapor partial pressure difference between the liquid surface and the air stream.

2.1.2 Bubble Column Dehumidifier (BCDH) Process

In this study we use a multi-tray bubble column dehumidifier (MBCD) as the dehumidifier along with the SGMD module to complete the desalination cycle. MBCD has

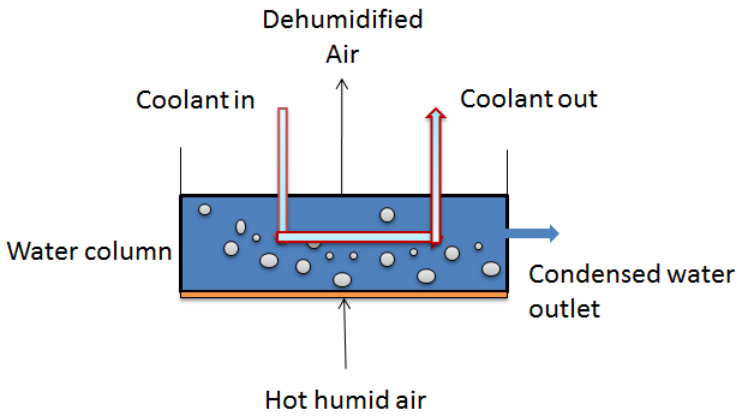

Figure 2-2: Schematic diagram of BCDH process

been proposed as an alternative to conventional dehumidifiers that use large metal areas for condensation and are therefore quite expensive. Figure 2-2 shows a schematic diagram of a single stage BCDH. The BCDH is an example of a direct contact dehumidifier where a hot moist air stream is bubbled through a column of pure water. The water vapor from the air bubbles condenses at the bubble surface and releases energy into the water column. By the time the air leaves the water column, it is cooled down and leaves close to the temperature of the water column. The heat released by the condensing vapor is removed from the water column by a coolant stream. In our system, the inlet saline feed water flowing inside a copper tube acts as the coolant. The energy released by condensation is therefore recovered and reused for preheating the feed water. Further discussion on the performance of BCDH compared to conventional dehumidifiers and the effect of high proportion of non-condensible gases is available in [22].

In Sec. 2.2, the modeling methodology is explained, followed by validation of the model in Sec. 2.3. Sec. 2.4 has a brief discussion on entropy generation within the individual components. Finally, results from simulations of the complete desalination cycle are discussed in Sec. 2.5.

2.2 Modeling

The numerical modeling was carried out using the commercial software, Engineering Equation Solver (EES) [23]. EES is an iterative numerical simultaneous eqution solver that uses accurate thermodynamic property data for air-water mixtures and water. The air-water mixture properties in EES are evaluated using formulae presented by Hyland and Wexer [24] and water properties are evaluated using the IAPWS 1995 formulation [25].

2.2.1 SGMD Module

Method

Khayet et al. [26, 27] have developed theoretical models of the transport processes within a SGMD module by considering the resistances to heat transfer, namely the feed and air side boundary layers as well as the membrane. Charfi et al. [28] modeled the module in two dimensions using the Navier-Stokes equation for both fluid streams with a suitable coupled boundary conditions at the membrane interfaces.

The modeling approach followed in this work is an extension of the technique presented in [2] for AGMD, DCMD and VMD systems. A one dimensional modeling approach is followed wherein property variations along the length direction are modeled using suitable conservation equations [29]. The fluid streams are assumed uniform in the width direction. Along the depth direction the effect of the boundary layers close to the membrane surface for either stream can not be ignored. These effects are captured by solving for the fluid properties at the membrane interface for both streams, and the interface values are also allowed to vary along the flow direction (length) of the module.

The advantage of this method is that it is computationally less cumbersome compared to a 2D Navier Stokes model. At the same time there is enough detail available to draw useful conclusions about system performance and to study the effect of various system variables.

Equations

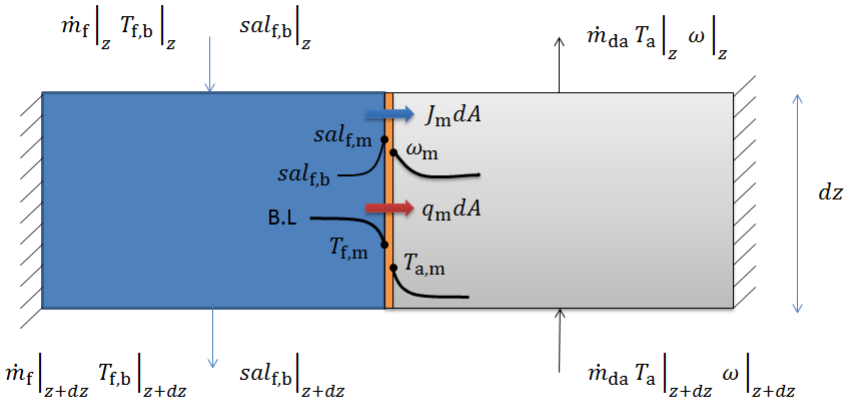

Figure 2-3: SGMD computational cell with heat and mass fluxes and associated boundary layers

Along the feed flow direction, the MD module is discretized into small control volumes of size dz, where $dz = L/n_{\text{cells}}$. The transport processes within and around one such section are shown in Fig. 2-3.

The main MD flux is modeled using a membrane property called the flux coefficient, B which is given by Eq. 2.1. B is considered constant for a particular system. For a particular membrane material, the value of B could vary under different operating conditions. The units of B are kg/m^2 s Pa.

$$J_m = B \times (p_{v,f,m} - p_{v,a,m}) \tag{2.1}$$

The feed side partial pressure of water vapor is the saturation vapor pressure over the liquid interface and is therefore only a function of liquid temperature and local salinity as given by Raolt's law:

$$p_{v,f,m} = P_{sat}(T_{f,m})\ x_{f,m} \tag{2.2}$$

On the air side, we use the ideal gas relationships to obtain $p_{\mathrm{v,a,m}}$ as shown in Eq. 2.3 and 2.4:

$$p_{\mathrm{v,a,m}} = P_{\mathrm{a}} x_{\mathrm{a,m}} \tag{2.3}$$

$$x_{\mathrm{a,m}} = \frac{\frac{\omega_{\mathrm{m}}}{MW_{\mathrm{v}}}}{\frac{\omega_{\mathrm{m}}}{MW_{\mathrm{v}}} + \frac{1}{MW_{\mathrm{a}}}} \tag{2.4}$$

We see that while on the feed side the vapor pressure is a strong function of temperature, on the air side, temperature of the air stream doesn't come into the picture. Most SGMD models [26] assume that the air stream is saturated at the inlet and remains saturated subsequently. Under those conditions, the partial pressure of water vapor in the air gap side is also only a function of the air temperature, since the state of saturated air is completely determined by its temperature. In our model, we do not make this assumption and hence in general, the partial pressure is not just a function of air's DBT.

On the feed side, mass and energy balance equations (Eq. 2.5,2.6) are solved:

$$\dot{m}_{\mathrm{f}}|_{z+dz} = \dot{m}_{\mathrm{f}}|_{z} - J_{\mathrm{m}} dA \tag{2.5}$$

$$\left(\dot{m}_{\mathrm{f}} h_{\mathrm{f,b}}\right)|_{z+dz} = \left(\dot{m}_{\mathrm{f}} h_{\mathrm{f,b}}\right)|_{z} - \left(J_m h_{\mathrm{v,f,m}} + q_{\mathrm{m}}\right) dA \tag{2.6}$$

Theoretically, for an internal flow Eq. 2.6 is valid only for bulk temperature defined as a mass averaged temperature over the cross sectional area of the flow. Here the equation is used with the value of the temperature outside the boundary layer as an approximation of the theoretical bulk value.

In addition to the mass flux, there is a heat flux across the membrane governed by the temperature difference across the membrane and the effective thermal conductivity of the MD membrane:

$$q_{\mathrm{m}} = \frac{k_{\mathrm{eff,m}}}{\delta_{\mathrm{m}}} (T_{\mathrm{f,m}} - T_{\mathrm{a,m}}) \tag{2.7}$$

The value of temperature at the membrane interfaces is determined as a function of the net heat transfer, heat transfer coefficient and free stream temperature value (Eq. 2.8, 2.9):

$$T_{\mathrm{f,m}} = T_{\mathrm{f,b}} - (J_{\mathrm{m}}(h_{\mathrm{v,f,m}} - h_{\mathrm{f,b}}) + q_{\mathrm{m}})/\alpha_{\mathrm{f}} \tag{2.8}$$

Note that while the entire energy loss from the feed side contributes to the temperature polarization on the feed side, only the sensible heat addition to the air stream is considered for temperature polarization on the air side. The latent heat of evaporation does not feature in the temperature polarization expression. Even under fogging conditions where a small amount of liquid water is formed in the air stream, the condensation and corresponding energy release is assumed to happen in the bulk since relative humidity computed at the membrane interface is always less than 1. The excess thermal energy carried by the vapor and the sensible heat input are transferred into the vapor stream from the membrane interface by convection:

$$T_{\mathrm{a,m}} = T_{\mathrm{a}} + (J_{\mathrm{m}}\, c_{p,\mathrm{v}}(T_{\mathrm{f,m}} - T_{\mathrm{a}})) + q_{\mathrm{m}})/\alpha_{\mathrm{a}} \tag{2.9}$$

The heat and mass transfer coefficients are evaluated using standard correlations for Nu and Sh for internal flows based on the Re, Pr and Sc numbers of the flow [30].

The salinity at the membrane interface on the feed side is evaluated using the film model of concentration polarization as

$$sal_{\mathrm{f,m}} = sal_{\mathrm{f,b}}\ \exp\left(\frac{J_{\mathrm{m}}}{k_{\mathrm{mass,f}}\,\rho_{\mathrm{f}}}\right) \tag{2.10}$$

Air Stream

In Eq. 2.4, we saw that the vapor partial pressure depends on the humidity ratio at the membrane interface. This is evaluated again using the film model as

$$\frac{\rho\left(\frac{1}{1+\omega}\right)}{\rho_m\left(\frac{1}{1+\omega_m}\right)} = \exp\left(\frac{J_{\mathrm{m}}}{k_{\mathrm{mass,a}}\,\rho_{\mathrm{a}}}\right) \tag{2.11}$$

Mass and energy balance equations are solved on the air gap side as well:

$$\dot{m}_{\mathrm{da}}\left(\omega|_z - \omega|_{z+dz}\right) = J_{\mathrm{m}} dA \tag{2.12}$$

$$\dot{m}_{\mathrm{da}}(h_{\mathrm{a}}|_z - h_{\mathrm{a}}|_{z+dz}) = J_{\mathrm{m}} h_{\mathrm{v,f,m}} dA + q_{\mathrm{m}} dA \tag{2.13}$$

When EES solves the above equations based on the mass and energy fluxes that enter the air stream, since the air-water mixture enthalpy function in EES is defined even for supersaturated states (relative humidity > 1), a check needs to be placed on whether supersaturation occurs. Whenever the air stream tends to become supersatured with water, the state of air is forced back to the saturation line at the same enthalpy in order to simulate fogging. Any excess water after this is done, is assumed to be in the liquid state as fog carried forward by the air stream.

The local entropy generation for the control volume located between z and $z+dz$ is evaluated to make sure that the second law of thermodynamics is satisfied everywhere locally.

2.2.2 Multi-tray Bubble Column Dehumidifier

Figure 2-4 shows a schematic diagram of a multi-tray bubble column dehumidifier. Hot moist air is bubbled through a series of water columns (stages), which are cooled by cool feed water. The condensed moisture from each stage is added to a subsequent stage and finally water at the lowest temperature (from stage 1) is extracted as pure product. Air leaves saturated at a temperature close to the that of the water column in each stage in a well designed BCDH. The water stream also gets heated to a temperature slightly below the temperature of water column. This is illustrated in Fig. 2-5. The difference in temperature between the air and coolant that leave a stage is called the terminal temperature difference (TTD) of the stage.

The main goal of the present study is to model the SGMD module in detail. Tow and Lienhard [31] have reported data from several bubble column dehumidifier experiments. Based on that data, a TTD of 1 °C is assumed for each stage of a well

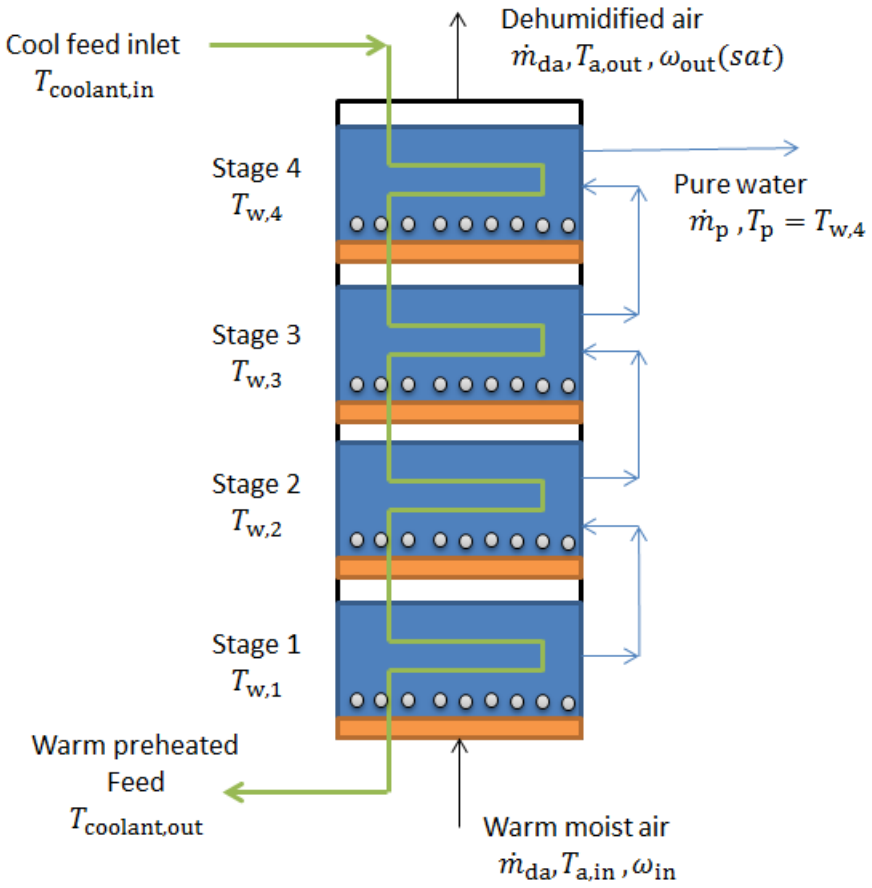

Figure 2-4: Schematic diagram of MBCD system with four stages

designed MBCD. In addition to this imposed condition, first law and mass conservation are solved for each stage and the stages are coupled together in order to solve for the overall outputs of the dehumidifier.

2.3 Validation

Charfi et al. [28] have published flux data from experiments conducted on a flat sheet SGMD module. Based on the data reported, the geometry of the experimental setup is estimated and programmed into the one dimensional model.

While the physical properties of the membrane such as porosity, mean pore size, and tortuosity have been reported, no value of membrane distillation mass transfer

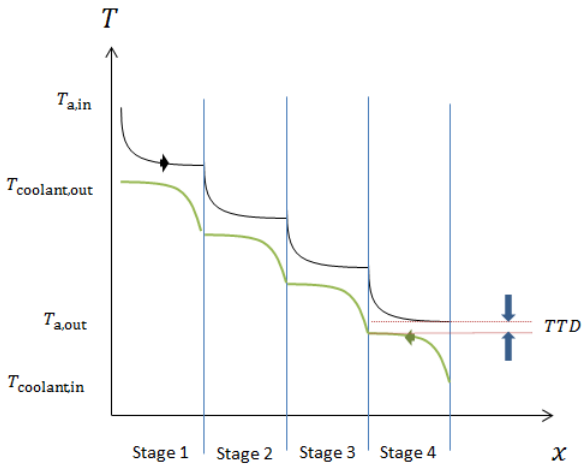

Figure 2-5: Temperature vs. position for a MBCD system showing the terminal temperature difference (TTD)

coefficient B is mentioned. The B value was fixed at 1.7×10^{-7} kg/m^2 s Pa a good match between the 1D model simulation results and experimental data is obtained. (Fig. 2-6).

Though additional experimental measurements are not included in the reference, simulation results from the 2D model are discussed. The overall match between experiment and the simulation has also been reported to be quite good ($R^2 = 0.9406$). The baseline conditions of their experiments and important physical parameters are collected in Tab. 2.1. Similar simulations are carried out using the one dimensional model described here.

The corresponding results from our model, at the same value of B determined earlier are included in Fig. 2-7. The flux decreases with an increase in air temperature since the inlet air stream was maintained at a saturated state in the experiment. As a result, an increase in temperature of the air meant a corresponding exponential increase in vapor partial pressure in the air and hence a reduction in the net driving force for mass transfer.

The SGMD flux increases with an increase in air stream velocity (Fig. 2-7(b)) since a higher air mass flow rate implies quicker vapor removal by the air stream. At very low air mass flow rates, the air stream is effectively humidified and heated close

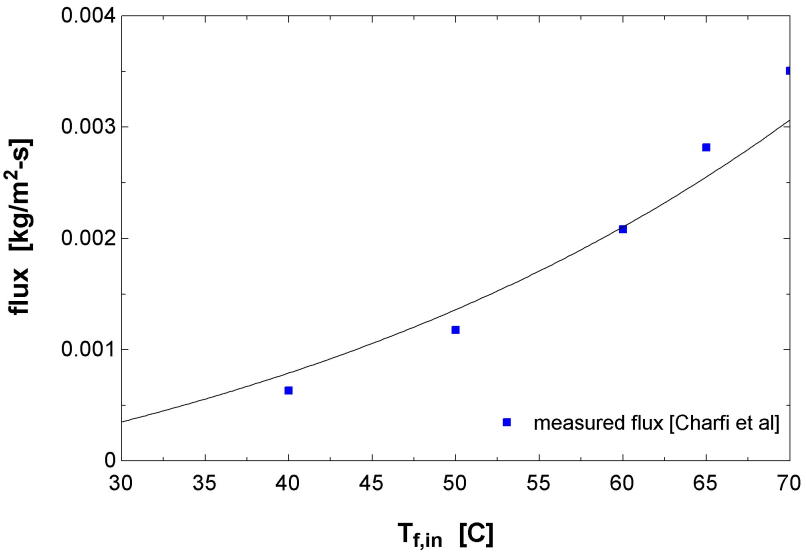

Figure 2-6: Flux vs. temperature of feed inlet compared with experimental data

to the temperature of the feed, at which point mass transfer driving force becomes very small. Under such conditions, if the air mass flow is increased, the outlet state of air will not change much. Net permeate production for the module is evaluated as

$$\dot{m}_{\mathrm{p}} = \dot{m}_{\mathrm{da}}(\omega_{\mathrm{out}} - \omega_{\mathrm{in}}) \tag{2.14}$$

While $\omega_{\mathrm{out}} \approx \omega_{\mathrm{sat}}(T = T_{\mathrm{f,in}})$ doesn't change much, the increase in $\dot{m}_{\mathrm{da}}$ would lead to a linear increase in flux. As the velocity increases however, the transport processes within the module will not be able to keep up and heat the air up to it's maximum value. As a result the rate of increase in flux drops with further increase in v_{a}. At higher velocities, the heat and mass transfer coefficients are also higher which results in lower difference in temperature and concentration across the boundary layers. In other words, the temperature and concentration polarization are reduced, contributing to an increase in flux.

The velocity of the feed has a smaller impact on flux. The flux increases with increase in v_f is owing to the reduction in temperature and concentration polarization in the feed channel.

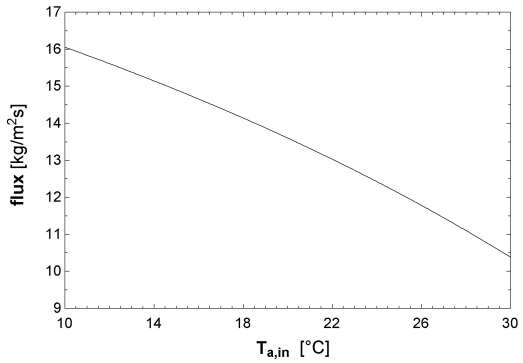

(a) Effect of saturated air inlet temperature

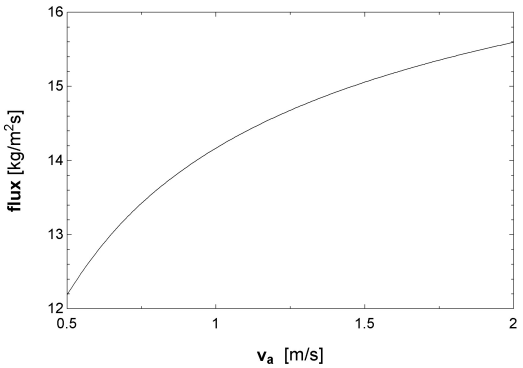

(b) Effect of air stream velocity

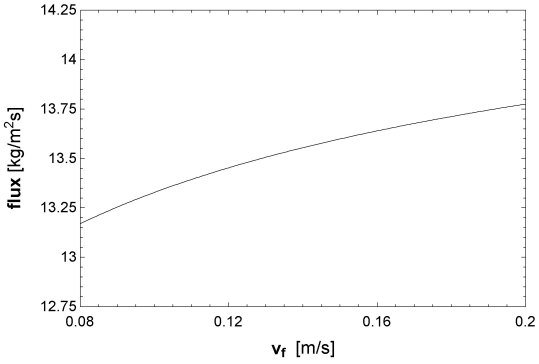

(c) Effect of feed velocity

Figure 2-7: Flux prediction

Table 2.1: Baseline values for validation test cases

S No	Variable	Value	Units
1	$T_{\mathrm{f,in}}$	50	°C
2	$T_{\mathrm{a,in}}$	20	°C
3	v_{f}	0.15	m/s
4	v_{a}	0.8	m/s
5	sal_{in}	0	ppt
6	L	0.068	m
7	w	0.08235	m
8	$d_{\mathrm{f}}, d_{\mathrm{a}}$	0.005	m
9	B	1.7×10^{-7}	kg/m^2 s Pa

Comparing with corresponding graphs from the 2D model (Fig. 5,7,8 of [28]), we see that the trends predicted by the two dimensional model are captured accurately by the present model. The absolute value of flux differs between the two models by a maximum of about 20%.

2.4 SGMD and MBCD System Analysis

2.4.1 Entropy Generation and GOR

The efficiency of a thermal desalination cycle is given by the Gained Output Ratio (GOR), a measure of the extent to which the supplied heat energy is reused within the system for evaporation and purification of the feed. GOR is defined as

$$GOR = \frac{\dot{m}_{\mathrm{p}} h_{fg}}{\dot{Q}_{\mathrm{in}}} \tag{2.15}$$

In this paper, h_{fg} for GOR evaluation is taken at 25 °C since MD uses low grade, low temperature heat sources. Other publications may use the value of h_{fg} at 100 °C. Since $h_{fg}(100°C) = 2.257 \times 10^6$ J/kg and $h_{fg}(100°C) = 2.442 \times 10^6$ J/kg, a GOR of 2.6 reported here would correspond to GOR=2.8 if enthalpy of vaporization at T_{bp} is used.

For desalination systems, it has been shown that minimizing specific entropy gen-

eration ($\dot{s}_{\text{gen}}$ is entropy generated per unit rate of permeate production) results in maximum GOR [5]. The entropy generation characteristics of the SGMD and MBCD systems are analyzed separately before they are put together to form a complete desalination system.

2.4.2 SGMD Module

As noted earlier, in this modeling framework, the air stream is not constrained to be saturated at all times. Instead, the air state can evolve as dictated by the actual heat and mass transfer driving forces. This enables us to analyze the effect of air stream preheating on entropy generation in the SGMD module. When the air stream is heated at constant total pressure, on a psychrometric chart, the state of air is displaced horizontally towards the right since there is no change in humidity ratio. Since the humidity ratio remains constant, the partial pressure of water vapor in in the air stream does not change. Therefore, while the mass transfer process is largely unaffected (except for secondary influences), the heat transfer between the streams is reduced. This would therefore lead to reduced entropy generation in the SGMD module.

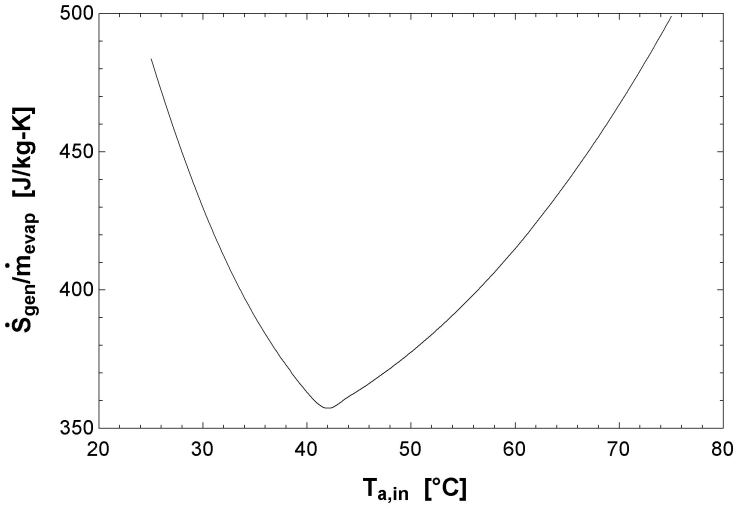

Figure 2-8: Specific entropy generation as a function of inlet air temperature. Humidity = $\omega_{\text{sat}}(25\,^{\circ}\text{C})$

Figure 2-8 shows this effect. The entropy generation within the module reduces and increases again with increase in inlet air DBT. The rate of decrease in entropy generation is very steep because of air state hitting the saturation dome and fogging occurring within the stream. The process path traced by the sweeping gas in the case of two inlet air temperatures (40 °C, 50 °C) is depicted on a psychrometic chart in Fig. 2-9. In Fig.2-9(a), the air stream gets heated and humidified until it hits the saturation dome. Thereafter, as discussed in Sec. 2.2.1, the air state is manually forced to follow the saturation dome. Total specific enthalpy of the air is used to choose the point along the saturation line. A small amount of liquid water is formed whose enthalpy is ignored while determining the air state ($h_{\mathrm{v}} \gg h_{\mathrm{l}}$), but the quantity of liquid water/fog is calculated and carried forward along with the air stream.

In Fig. 2-9(b) on the other hand, the air is seen to be almost exclusively humidified(the state of the air stream evolves vertically upward). Initially the air loses DBT as some heat transfer occurs to the water stream which is at a lower temperature. In the latter part of the of module, the air is heated and humidified by the feed stream.

The flow evolution along the length of the module can be visualized better using the help of a temperature vs. position plot. In Fig. 2-10(a), we see that the water DBT denoted by T_{a} does not vary much initially as it flows from $L = 12$ m to about 2 m. At this point, the air stream becomes saturated and it starts following the saturation curve with $T_{\mathrm{a}} = T_{\mathrm{wb}}$. On the other hand, in Fig. 2-10(b), while the DBT does not change over the length of the module, the wet bulb temperature increases steadily.

In both the graphs, the temperatures of the air and feed at the membrane interface are almost equal. This shows that there is significant temperature polarization in both streams. Another effect of this is that there is very little sensible heat transfer from the feed to sweeping gas ($q_{\mathrm{m}} \approx$ 30-40 W/m^2). Any sensible heat transfer, in MD is considered a loss. Interestingly, while the high air side temperature polarization adds a thermal resistance within the stream, it is beneficial in reducing the net sensible heat loss from the feed.

Figure 2-11 shows the vapor pressure difference across the membrane which drives

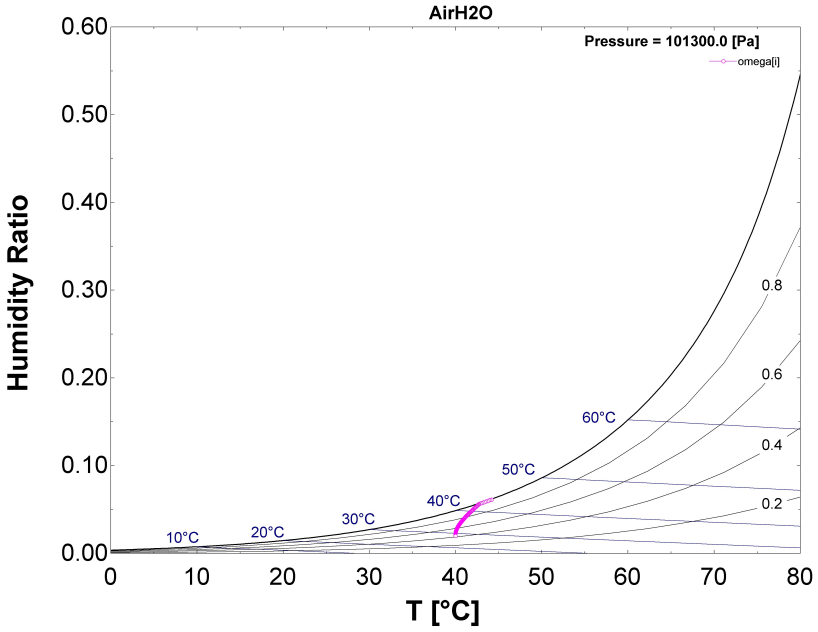

(a) Air inlet temperature = 40 ° C

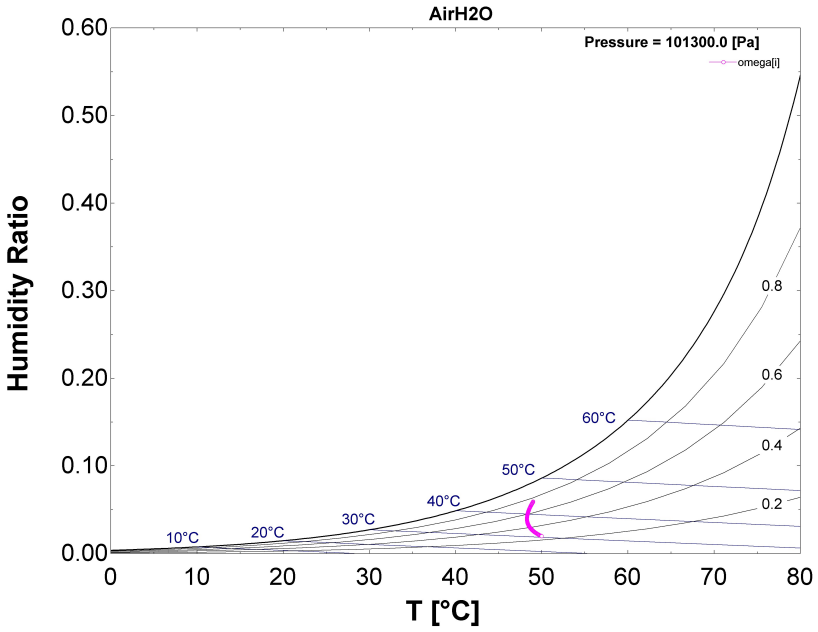

(b) Air inlet temperature = 50 ° C

Figure 2-9: Air stream state

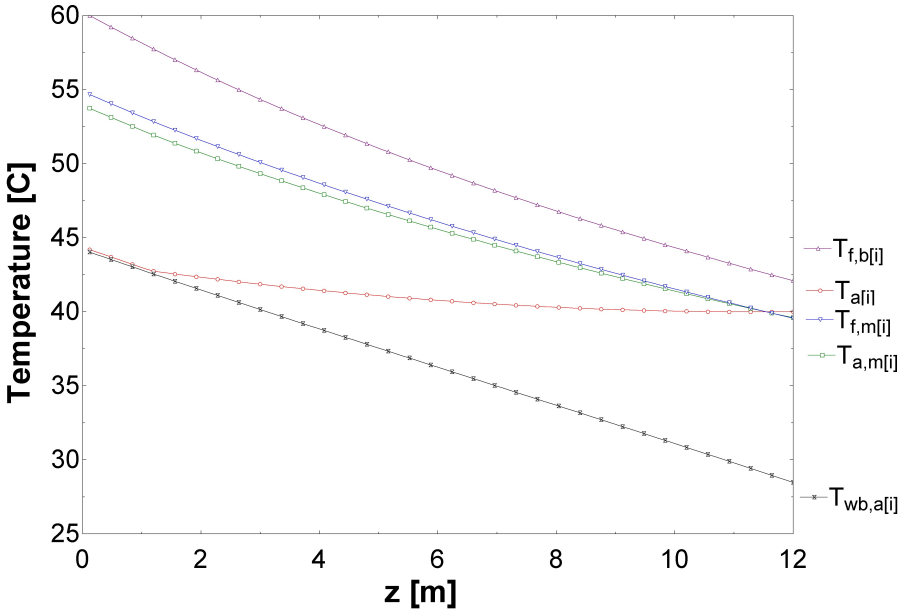

(a) Air inlet temperature = 40 °C

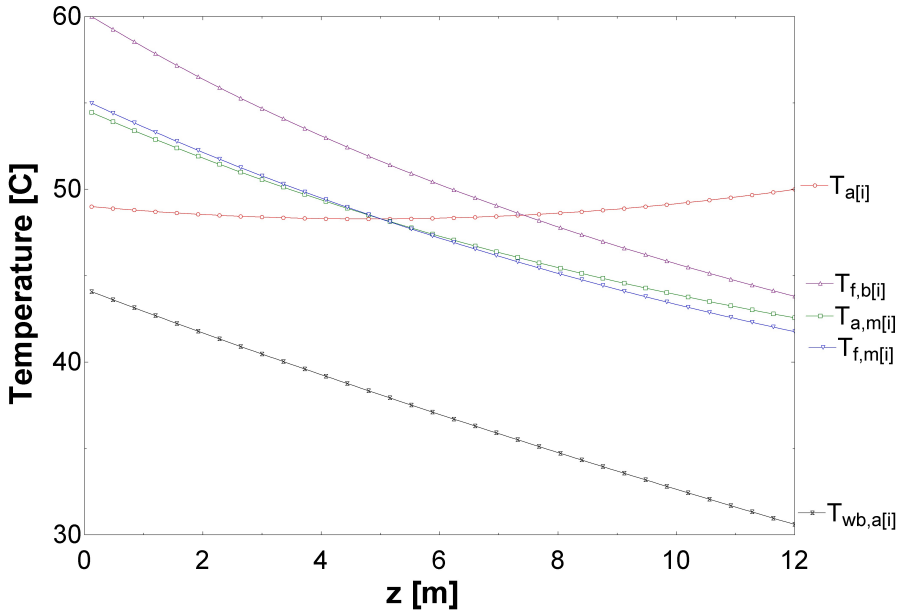

(b) Air inlet temperature= 50 °C

Figure 2-10: Temperature vs. position

transfer of pure water vapor. As explained earlier, the increased DBT of the inlet air does not affect the vapor pressure of the air stream and hence the mass transfer processes in the two cases are nearly identical. In Fig. 2-11(b), we see that in the lower specific entropy production case, the air stream vapor pressure at the exit is slightly higher indicating a small increase in overall flux. These graphs characterize the physical processes within the module and help confirm that the model captures the phenomena accurately.

2.4.3 Multi-tray Bubble Column Dehumidifier

The specific entropy generation in the proposed MBCD model is plotted in Fig. 2-12. As expected, the specific entropy generation has a minima with respect to changing $\dot{m}_{\mathrm{da}}$ with other parameters fixed. Combined heat and mass transfer devices such as dehumidifiers (and humidifiers) produce minimum entropy when the heat capacity rates of the two streams are matched [32].

The irreversibility within the device increases with increase in $T_{\mathrm{a,in,BCDH}}$ under these conditions [2-12(b)]. This is expected since with an increase in inlet air temperature, both heat and mass transfer driving forces increase in the system.

2.5 Cycle Analysis

A schematic diagram of the overall desalination cycle is illustrated in Fig. 2-13. The two models are combined by matching their inlet and outlet states suitably in EES. The configuration chosen is a closed air open water configuration. Cold water is taken into the dehumidifier and used to as the coolant. As it passes through, the enthalpy of condensation is transferred from the water column into the cold water stream and it is preheated. The feed water then goes through a water heater where it is heated to the cycle top temperature. In this study, the cycle top temperature is fixed and hence the heat input varies depending on the extent of preheating. The hot water then goes through the SGMD module. Here evaporation causes cooling of the feed. The minimum temperature to which the feed can get cooled is the wet

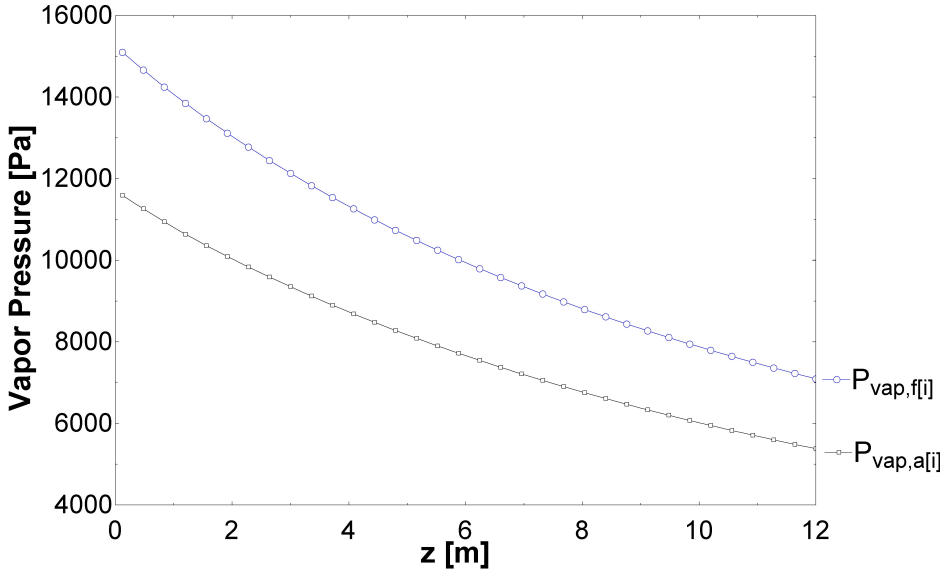

(a) Air inlet temperature = 40 °C

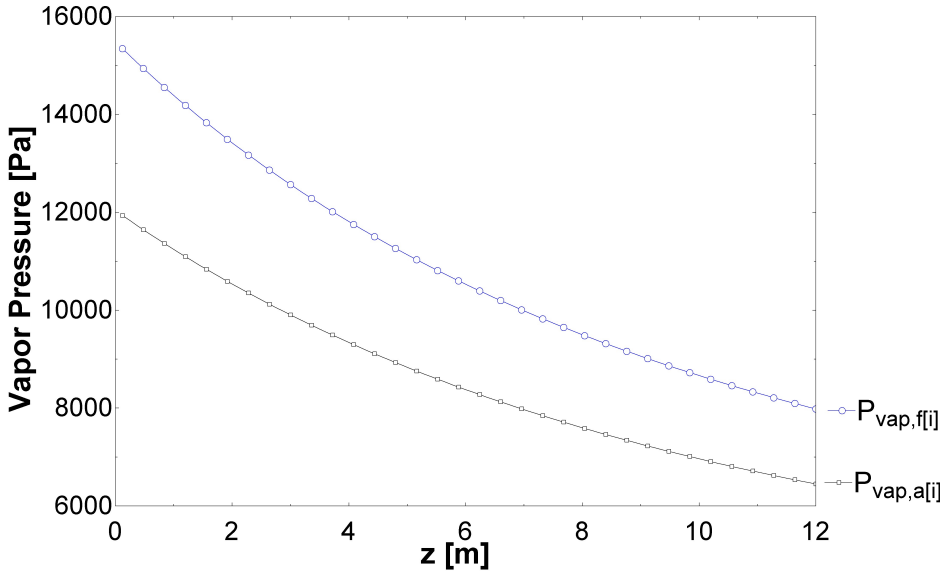

(b) Air inlet temperature = 50 °C

Figure 2-11: Vapor pressure vs. position

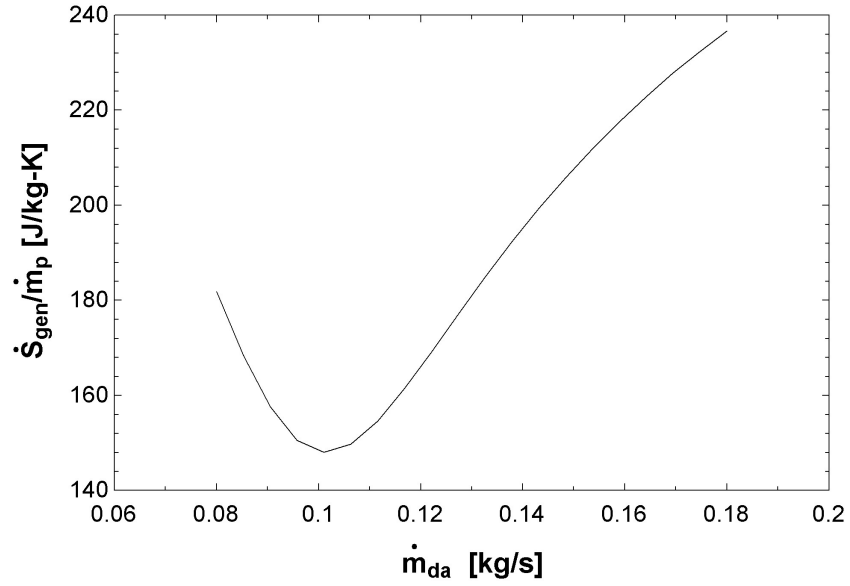

(a) Effect of $\dot{m}_{da}$

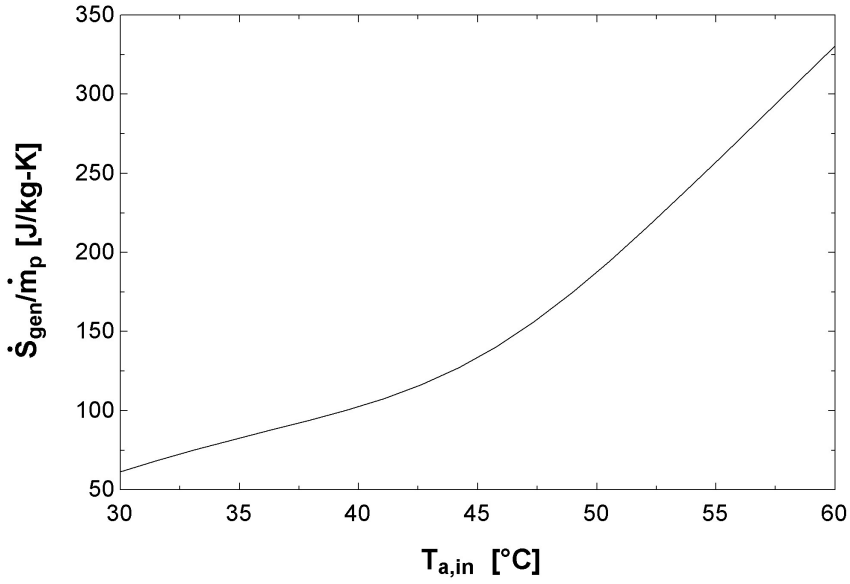

(b) Effect of $T_{a,in,BCDH}$

Figure 2-12: Specific entropy generation in a MBCD. ($T_{\mathrm{a,in}} = 50\,^{\circ}\mathrm{C}$, $\dot{m}_{\mathrm{c}}$= 0.189 kg/s, $T_{\mathrm{c,in}}$= 25 °C)

bulb temperature of the air inlet into the SGMD module and as it approaches this temperature the driving force for mass transfer will reduce. The brine that exits the SGMD module is disposed.

The air stream forms a closed loop as the name of the configuration indicates. Air enters the SGMD module and is humidified by addition of vapor from the feed stream. In the process, the temperature of the air also increases. This stream is then taken into the MBCD where it is bubbled through multiple water baths using spargers. As the bubbles rise, air is cooled and excess water vapor condenses into the water. The air that exits the MBCD is then fed back into the SGMD module.

Since the two devices are now coupled, the number of degrees of freedom is reduced. The temperature of the air stream is no longer an input to the system. The mass of the liquid streams are also equal in both the devices. We previously observed that $\dot{s}_{\text{gen}}$ is minimized in the MBCD at a particular value of $m_{\text{r}} = \dot{m}_{\text{da}}/\dot{m}_{\text{f}}$. Similarly the SGMD system would produce minimum entropy at a different value of m_{r}. Since the entropy generation in both devices is of the same order of magnitude, the overall system performance and the effect of the system inputs would be a result of the combined effect of both devices.

The baseline parameters for the simulations are given in Table 2.2. Each of the parameters are varied around their baseline value keeping the other variables constant to understand their effect on the overall cycle GOR.

2.5.1 Mass Flow Rates

The mass flow rates are important parameters in the SGMD desalination system. With both the SGMD module and the MBCD irreversibilities being functions of m_{r}, the overall system too is very sensitive to the mass flow rates of feed and air. In addition to its effect on the thermodynamics as described above, the mass flow rate of a stream also affects the Reynolds number and thereby the Nusselt and Sherwood number of the stream in the SGMD module. Through its effect on the Nu and Sh, an increase in mass flow rate of either stream would lead to a monotonic increase in GOR of the cycle. The thermodynamic effect dominates as is seen in Fig. 2-14, with

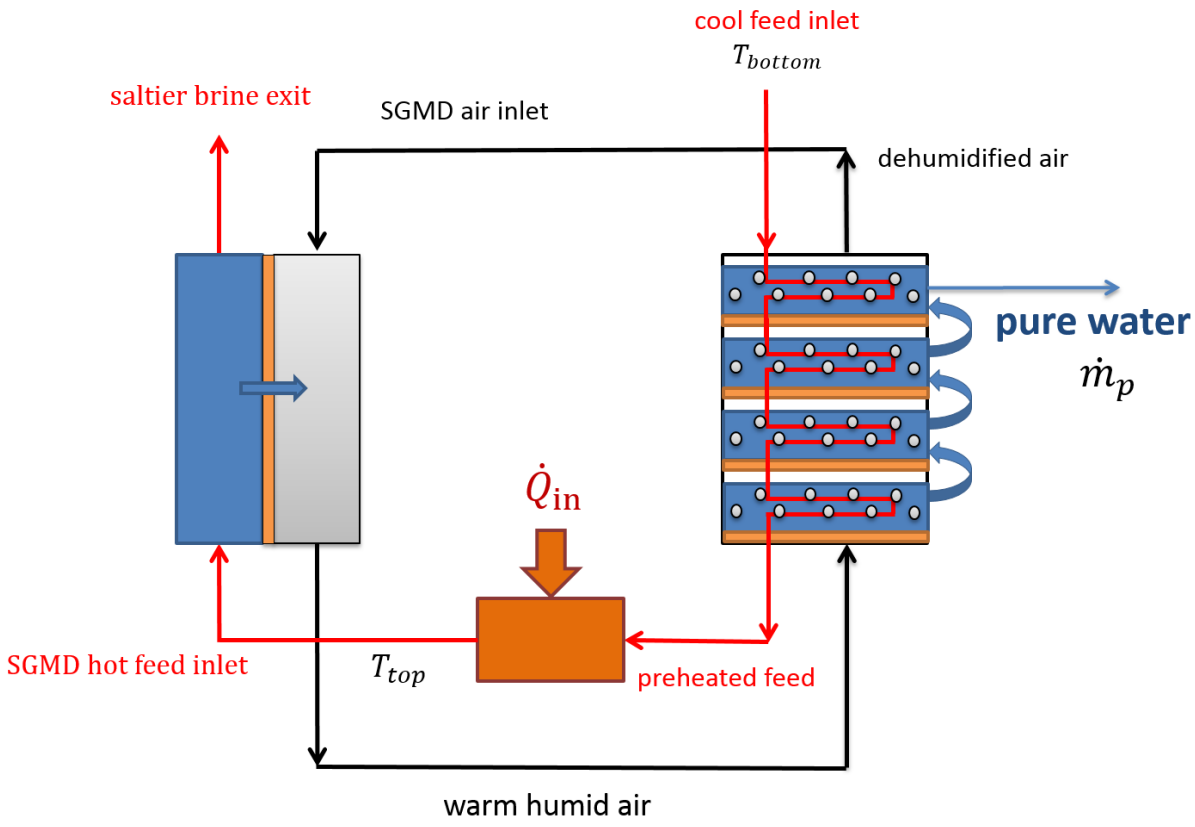

Figure 2-13: Complete SGMD-MBCD desalination system

the GOR attaining a maximum at a particular value of feed and air mass flow rate and reducing thereafter.

2.5.2 Temperatures

SGMD feed inlet

The temperature of the feed input the SGMD module is a design variable and is the cycle's top temperature. Figure 2-15 shows the effect of cycle top temperature on GOR. When all other parameters such as system geometry and flow rates are fixed, GOR is maximized at $T_{\text{f,in}} = 70°$ C.

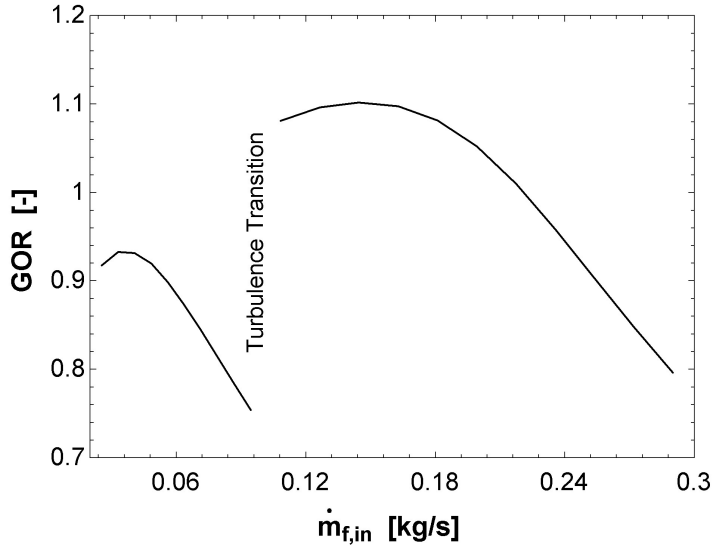

(a) Feed side. Discontinuity due to transition to turbulence

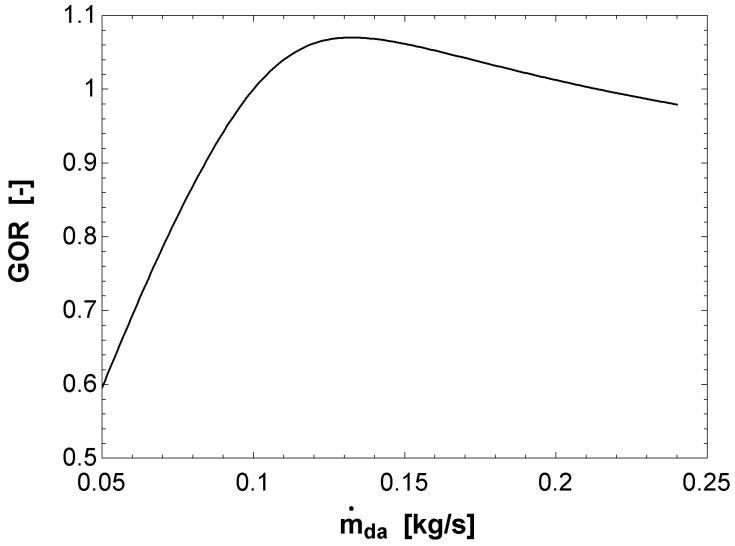

(b) Air side

Figure 2-14: GOR dependence on mass flow rates

Table 2.2: Baseline values of SGMD desalination system

S No	Variable	Value	Units
1	$T_{\mathrm{f,in}}$	60	°C
2	$T_{\mathrm{cold,w,in}}$	25	°C
3	$\dot{m}_{\mathrm{f,in}}$	0.189	kg/s
4	$\dot{m}_{\mathrm{da}}$	0.1345	kg/s
5	$sal_{\mathrm{f,in}}$	30	ppt
6	L	12	m
7	w	0.125	m
8	d_{f}	0.004	m
9	d_{a}	0.04	m
10	B	16×10^{-7}	kg/m^2 s Pa
11	TTD	1	°C
12	$n_{\mathrm{BCDH,stages}}$	6	-

Coolant

The temperature of the coolant (feed inlet from the environment) has a smaller effect on GOR (Fig. 2-16). Since the baseline mass flow rates were chosen such that GOR is maximized, the GOR is maximum close to $T_{\mathrm{c,in}} = 25\,^{\circ}\mathrm{C}$.

2.5.3 Geometry

Geometry of the SGMD module affects the transport processes within significantly. Figure 2-17 shows the influence of the effective length and width of the module on GOR. Both length and width affect the total available membrane area. While the length does not affect the cross section and hence the flow velocity, changing the width introduces these additional effects as well. At the baseline operating parameters and module dimensions (chosen to be in the range of other commonly studied MD systems [2]), the SGMD module design is not optimized since $T_{\mathrm{f,out}}$ from the module is much higher than the wet bulb temperature of the air inlet (see Fig. 2-10, for example). Increasing the area of the membrane is similar to increasing the area of a heat exchanger. The total heat and mass transfer increase and the overall irreversibility in the system decreases with an increase in both width and effective length.

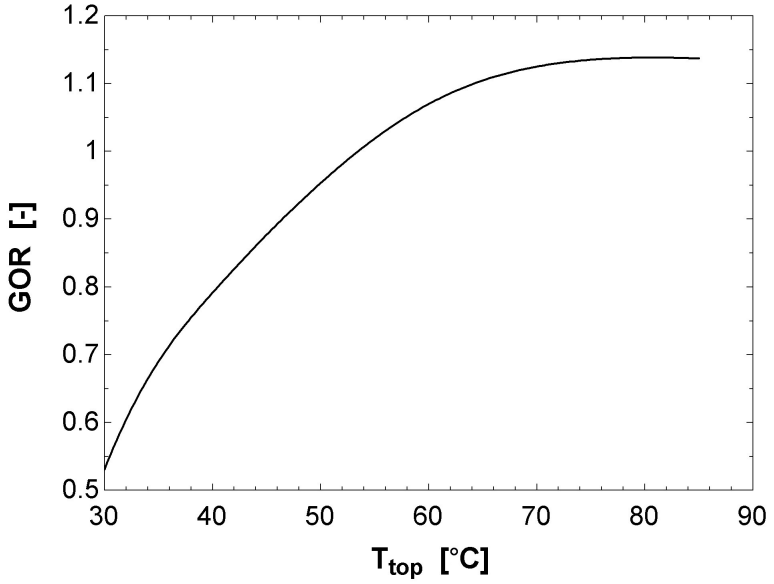

Figure 2-15: GOR dependence on cycle top temperature

Figure 2-17(a) shows that increasing the length of the module results in a large increase in GOR. With the flow characteristics and mass flow ratios unaltered, the increase is predominantly owing to better usage of the heat in the feed stream. With increase in length, $T_{\mathrm{f,out}}$ decreases and the mass transfer occurs over a smaller Δp_{v}.

In Fig. 2-17(b), the gap in the graph corresponds to a change of feed flow regime to laminar as the cross sectional area increases with increase in width. The GOR increase is observed over a smaller range in the case of width as compared to length. This is because of the other being held constant. When the width is increased to 3 m, the length is held constant at 12 m resulting in an overall membrane area of 36 m^2. On the other hand, to reach the same membrane area with a width of 0.125 m, the length must be 144 m. Note that at an effective length of 144 m, the GOR achieved is higher than at width of 3 m though the overall membrane area is the same. This is because an increase in length does not affect the flow regime in the module and the feed and air Reynolds numbers remain the same ($\mathrm{Re_f} \approx 5000, \mathrm{Re_a} \approx 4.4 \times 10^4$). On the other hand, the Reynolds numbers and hence heat and mass transfer coefficients of both streams reduce with an increase in width. In a real system one would have to

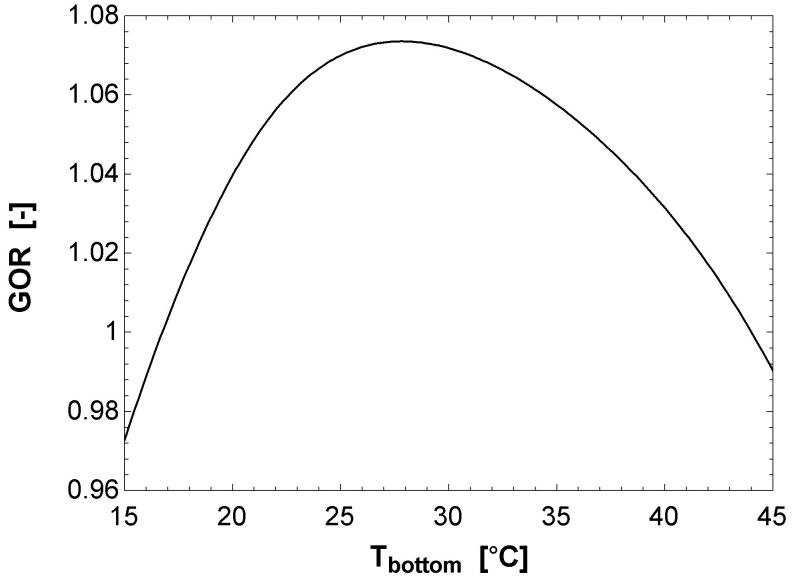

Figure 2-16: GOR dependence on cycle bottom temperature

pay for the increased GOR in the longer module in the form of a much larger pressure drop and hence pumping power, compared to the wider module which has a slightly lower GOR.

The effect of the depth of the two channels is illustrated in Fig. 2-18. The effect of increasing d is similar for both the streams. The membrane area remains unaltered and the only effect is on cross sectional area and therefore on the transport processes and boundary layers in the two streams. Correspondingly, the change in GOR over the range of d_{f} and d_{a} is smaller than in the case of the other dimensions. An increase in depth of the channel leads to higher boundary layer resistances and therefore smaller GOR. Figures 2-18(a) and 2-18(b) suggest that polarizations in both streams are significant. The temperature polarization in the feed stream and concentration polarization in the air stream have maximum impact since they directly affect the mass transfer driving force by reducing the vapor pressure difference substantially. The concentration polarization on the feed side can have a significant effect too, especially under laminar flow conditions.

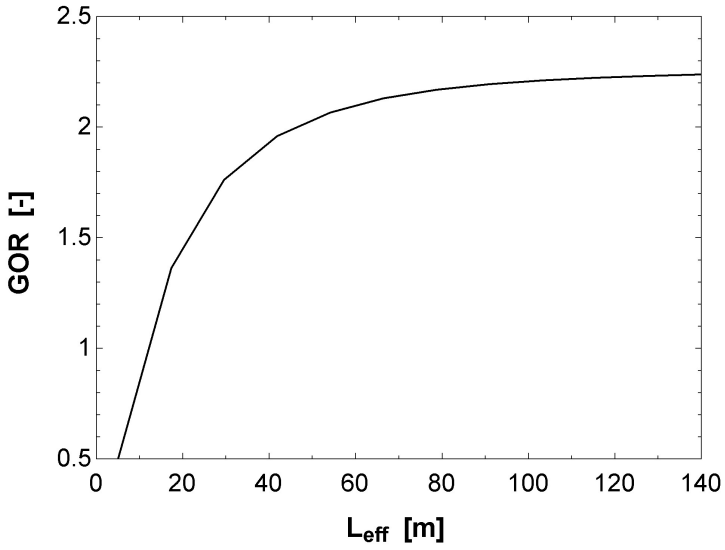

(a) Effective length

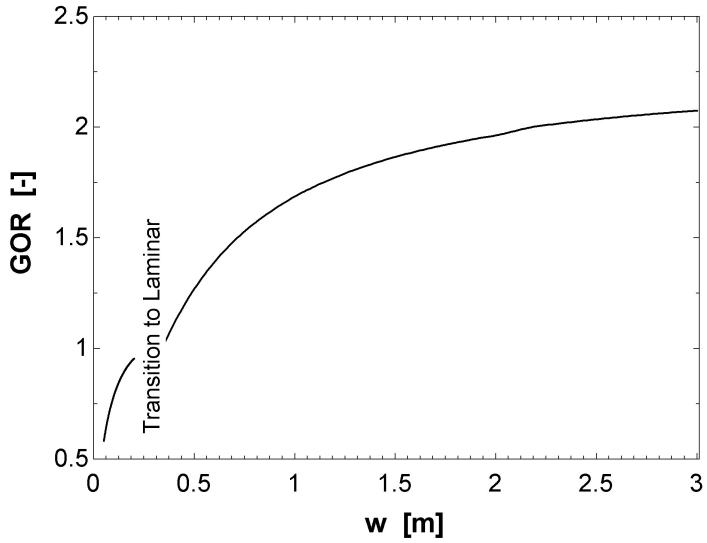

(b) Width

Figure 2-17: GOR dependence on length and width

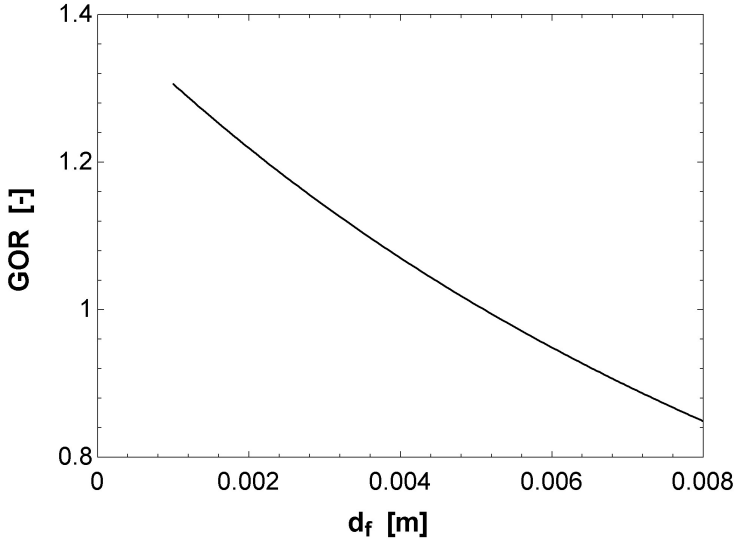

(a) Feed side

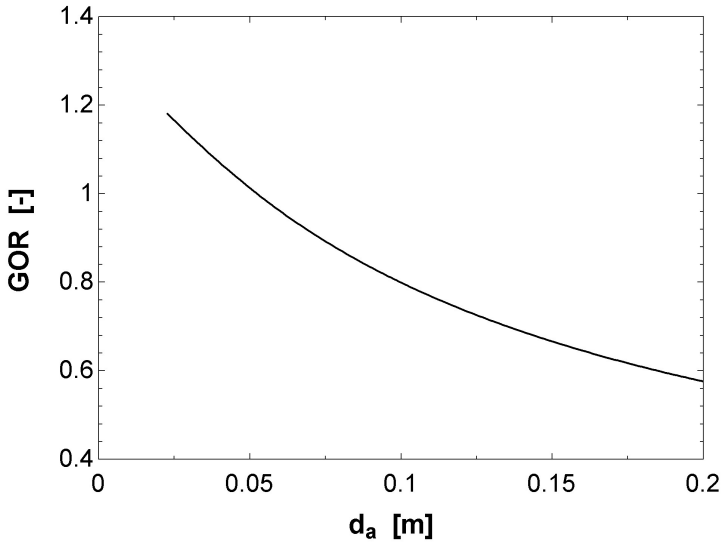

(b) Air side

Figure 2-18: GOR dependence on channel depth

2.5.4 Dehumidifer Effectiveness

MBCD effectiveness increases with number of stages. The number of stages also determines the pressure drop through the system and the cost. The marginal gains in GOR with increase in the number of stages of the dehumidifier is presented in Fig. 2-19.

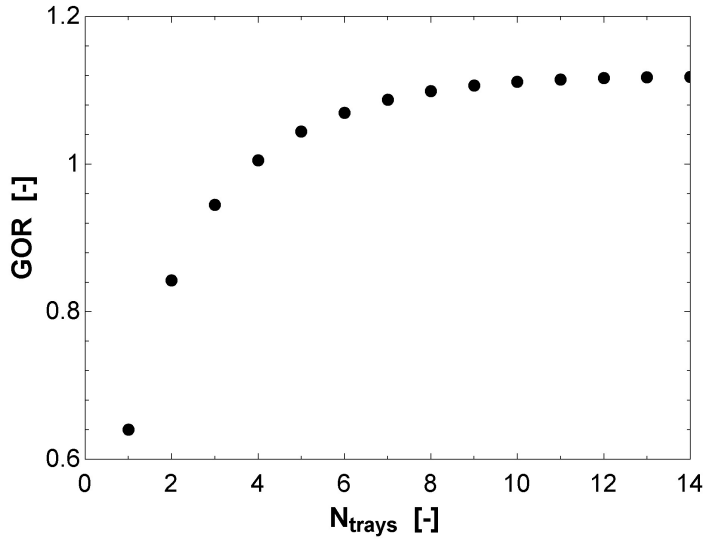

Figure 2-19: Effect of number of BCDH stages

2.5.5 Membrane Properties

The B value of the membrane directly influences the flux in MD processes. With higher B giving rise to higher flux, one could use smaller devices. In other words, if the membrane area is held constant and the membrane permeability is increased, we can expect to see an increase in efficiency as shown in Fig. 2-20. It should be noted that higher permeability alone does not guarantee good thermal efficiency (GOR vs. B graph plateaus beyond a point). While high permeability membranes will help, they are not a substitute for thermodynamic analysis and cycle design.

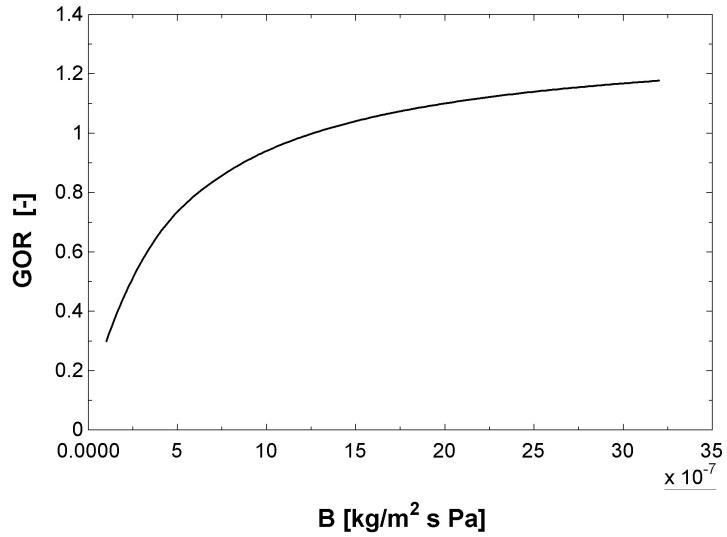

Figure 2-20: Effect of membrane permeability

2.5.6 Further Improvements

In the preceding sections, the effect of each independent variable was studied keeping other parameters fixed. This yields a GOR just over 2 with large enough membrane area (≈ 36 m^2). Further improvements to GOR are possible when all the independent variables are allowed to change. For example, Fig. 2-21 shows the effect of feed mass flow rate on GOR when the module effective length is set as 60 m. The maximum GOR attained is close to 2.6 in this case.

2.6 Conclusions

A one-dimensional numerical model of the heat and mass transfer processes occurring in a SGMD module is developed. The model can take in both saturated and unsaturated air as input and the process path is evaluated using the membrane distillation coefficient B. Entropy generation within the SGMD module is studied with respect to changes in the system variables.

The model has been used to study the energy efficiency of the SGMD based desalination cycle using a multi-tray bubble column dehumidifier to recover pure water.

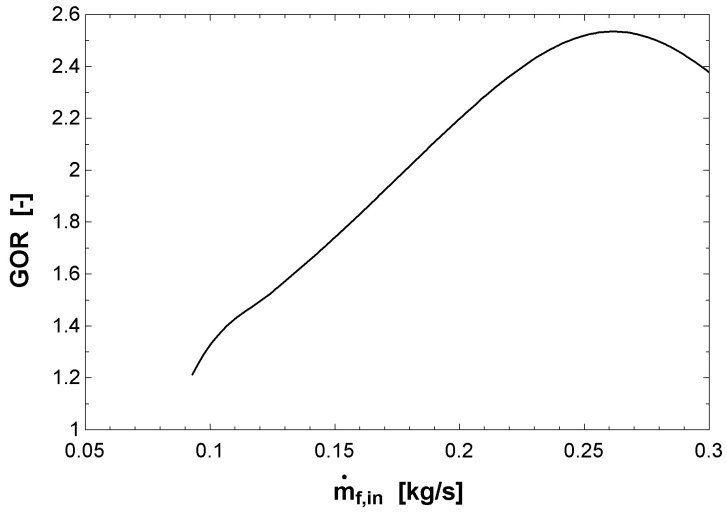

Figure 2-21: GOR vs. feed mass flow rate. $L = 60$ m

Entropy generation in the dehumidifier is found to be important, often competing with the SGMD module in deciding the optimum operating conditions.

The boundary layer resistances and associated temperature/concentration polarizations are found to have a significant impact on reducing thermal efficiency. Improvements in mixing within the streams such as the use of suitable spacers of baffles can lead to further improvements in efficiency.

This model can be a useful tool for designing optimal desalination cycles under a set of design constraints. The effect of each independent variable on GOR was studied. For a longer module, a maximum GOR in excess of 2.5 is observed with changing feed mass flow rate. Now that the effect of each individual process parameter is understood, further optimization is possible to look for operating conditions that yield global maximum GOR.

Chapter 3

Experimental Design of Air Gap Membrane Distillation System for Fouling Tests

David E. M. Warsinger contributed to this chapter.

Abstract

Experimental investigation of inorganic salt fouling in MD is a useful tool to map regions of safe operation where MD can be used over long periods of time. In relation to this, the experimental design of an air-gap membrane distillation apparatus with well defined feed thermal, concentration and flow conditions is described in this chapter. The desirable features of each component of the experimental setup are discussed and solutions to practical challenges faced during the experiments are illustrated. Experiments were conducted over a wide range of temperature, flow rate and NaCl feed salinity conditions. Theoretical modeling of the heat and mass transport processes was able to successfully predict the dependence of flux on system input parameters. This model can therefore be used in the future to design specific membrane fouling tests with known conditions at the fluid membrane interface.

3.1 Introduction

One of the frequently quoted beliefs about the membrane distillation desalination process is its relatively higher resistance to fouling [33]. Membrane distillation being

a thermally driven technology has very high potential in the market for treatment of high salinity feed streams where reverse osmosis cannot be used [34]. Under these conditions, the importance of fouling resistance becomes multi-fold. Characteristic high salinity feed solutions include RO brine solutions at about 70 ppt salinity and hydraulic fracturing flow back water that span a wide range of composition and salinities. In industrial operation MD membranes are likely to be exposed to several types of potential foulants including organic, inorganic and biological substances. Of these, inorganic crystalline precipitation scaling is relatively better understood in other engineering systems and especially in other membrane systems [9].

Quantifying fouling characteristics of various salts under membrane distillation process operating conditions will be extremely useful in finding out safe operating regimes for a given feed stream composition. Knowing the rate of fouling and related flux decline, we can better estimate cleaning frequency and costs when designing systems. The efficiency of anti-foulants and cleaning methodologies can also be studied in a targeted and scientific manner using such an experimental apparatus.

3.2 Design Criteria

In any real MD system, the feed stream would start off relatively dilute and will get progressively concentrated as it loses pure water. As a result, a common observation in RO and other systems is that the far end of the membrane is more susceptible to inorganic fouling and this is likely to be true in MD as well. In order to be able to test the fouling conditions under a wide variety of well characterized operating conditions though, it is challenging to use a realistic MD system since the internal dynamics of temperature and concentration along the length of the module can only be, at best, estimated using analytical or numerical models of the system operation. On the other hand, we want to generate a map of temperature and concentration conditions and corresponding potential foulants in MD, wherein it is important to know with some degree of certainty the actual conditions at the membrane area of interest.

In order to satisfy these requirements, a small scale MD setup is chosen (Fig. 3-1).

Since the effective membrane area is small, the feed flow rate, temperature and salinity do not really vary by much from the inlet to the outlet of the module. Measured rate of fouling in such a system would correspond to a local region along the feed flow direction in a large scale system. By changing the three variables independently it is possible to map the whole domain of temperature, salinity and flow rates and therefore infer the local fouling rates in a real setup.

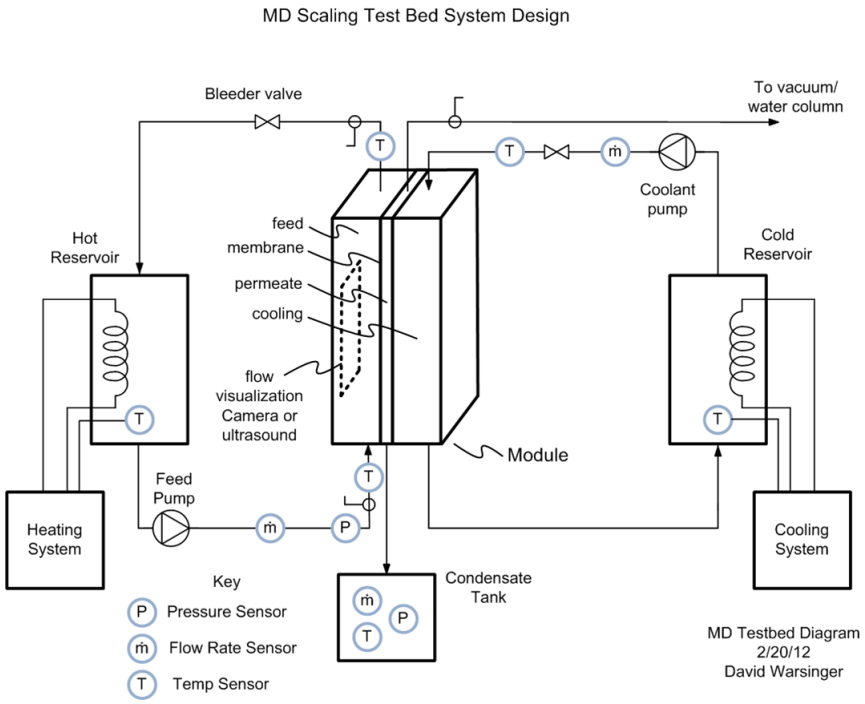

Figure 3-1: A schematic diagram of the MD experimental setup

3.2.1 Module Type

Several MD module configurations have been designed and tested, including plate and frame, spiral wound and hollow fiber designs. Of these, the plate and frame design is the most frequently implemented and has been chosen for this study as well. This configuration is the easiest to build at the lab scale with flat membranes being available on the market that can be used directly. Observing scale in situ is easier on a flat membrane that is directly accessible and can be visualized from outside. Plate

and frame also allows for easy removal, cleaning and replacement of membrane which is an essential feature of a fouling analysis experiment [35].

3.2.2 MD Configuration

Several types of MD systems have been studied, including the direct contact, air gap, sweeping gas and vacuum or reduced pressure systems based on the design of the permeate side of membrane. Summers et al. [2] have analyzed these single stage systems and evaluated their performance in terms of energy recovery. AGMD modules were shown to have highest potential for optimization and high energy efficiencies, as shown in Fig. 3-2 where for equal membrane area, at large effective lengths, the GOR of AGMD exceeds both that of DCMD and VMD configurations.

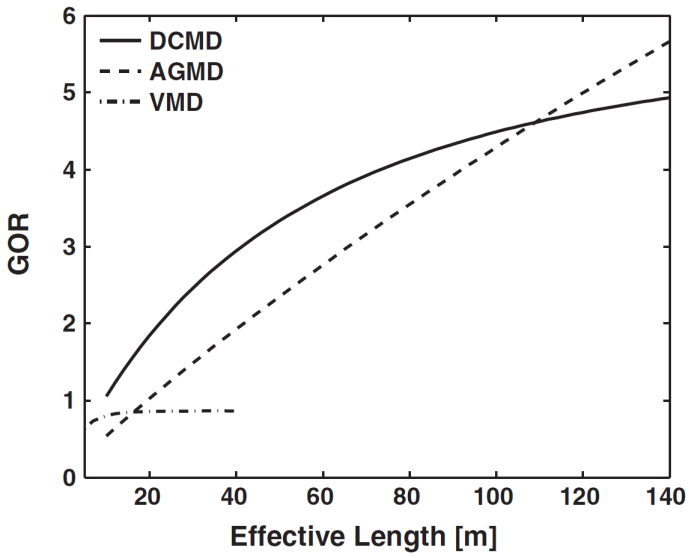

Figure 3-2: GOR comparison between single stage MD configurations [2]

There are other advantages that AGMD enjoys over DCMD. In AGMD, the produced pure water stream is collected independent of the cooling water, whereas in DCMD, the product water condenses directly into the cooling water stream. As a result, product water flux can be measured directly and with much better accuracy in AGMD. Leakage through the membrane can also be detected earlier since an increase

in salinity of the collected permeate is observed immediately, whereas in DCMD the salt water that leaks will get diluted by the pure cold water.

3.2.3 Feed Reynolds Number

MD studies in the literature are carried out over a wide range of flow rate conditions. The Reynolds number of the feed flow is an important variable in more ways than one. The flow condition being laminar or turbulent is a function of the Reynolds number and would control the heat and mass transfer coefficients within the channels and correspondingly the extent of temperature and concentration polarization. In practice it is likely that systems would run at slightly turbulent conditions to make use of the membrane area quite effectively, by reducing the boundary layer resistances.

In addition to affecting the transport properties, the velocity of fluid flow within the module also plays a role in the kinetics of the scaling process. Inorganic fouling is considered to be a sequential process where a seed of fouling material attaches to the membrane, followed by growth of crystals. Crystals may be sheared off by the flow, and the balance between the growth and removal processes defines an equilibrium condition for fouling. High flow rates are likely to increase the rate of scale removal from the membrane surface [36].

The feed flow channel has a depth of 4 mm. The Reynolds number can be varied from about 1000-5000 in our experiment with a corresponding feed average velocity range of 0.06-0.66 m/s.

3.2.4 Membrane Area

We use a 16 cm by 12 cm area of active membrane. The total active area of membrane used is important since under fixed temperature conditions, the flux is linearly related to the effective membrane area.

$$J = B \times \Delta P_{\text{vap}} \times A \tag{3.1}$$

The relative error in flux measurement would decrease at high values of absolute

water production. Since flux decline is one of the most commonly used metrics to infer fouling, measuring flux with higher accuracy is desirable. As a result, we use a larger membrane area than is used in many other coupon type test setups [37].

3.2.5 Air Gap

The air gap thickness is by far the most sensitive variable determining MD flux and performance (Table 3.1). Since the transport of water vapor across the gap to the condensing surface is predominantly by diffusion (Eq. 4.2), an increase in the air-gap thickness translates to an increased mass transfer resistance and a reduced flux. In our setup, the air gap is designed to be 1mm wide. In practice, the air gap thickness is a parameter that is hard to control (Section 3.5.2). During operation, the MD membrane experiences large pressure on the feed side and in AGMD, 1 atm pressure on the air gap side. As a result the membrane would collapse onto the condensing plate in an open air gap configuration. To prevent this, we use a spacer on the air-gap side to support the membrane. A discussion of several spacer alternatives can be found in [38]. Based on trial and error, Summers suggests the use of a woven mesh spacer that provides support equally in the horizontal and vertical directions.

Table 3.1: Uncertainty in flux as a function of uncertainty in measured parameters (using EES). An uncertainty of 0.05 mm in d_{gap} contributes to more than 75 % of the uncertainty in flux

$$\dot{m}_p = 8.229 \times 10^{-2} \pm 3.794 \times 10^{-3} \text{ [g/s]}$$

$B = 1.6 \times 10^{-6} \pm 3.8 \times 10^{-8}$ [kg/m^2 Pa s]	$\frac{\partial \dot{m}_p}{\partial B} = 6.356$	0.29%
$d_{\text{gap}} = 7.5 \times 10^{-4} \pm 5 \times 10^{-5}$ [m]	$\frac{\partial \dot{m}_p}{\partial d_{\text{gap}}} = -6.549 \times 10^{-2}$	75.17%
$\dot{m}_{\text{c,in}} = 1.773 \times 10^{-1} \pm 5 \times 10^{-2}$ [kg/s]	$\frac{\partial \dot{m}_p}{\partial \dot{m}_{\text{c,in}}} = 3.33 \times 10^{-6}$	0.19%
$\dot{m}_{\text{f,in}} = 2.558 \times 10^{-1} \pm 3 \times 10^{-2}$ [kg/s]	$\frac{\partial \dot{m}_p}{\partial \dot{m}_{\text{f,in}}} = 4.126 \times 10^{-5}$	10.64%
$S_{\text{in}} = 200 \pm 6$ [g/kg]	$\frac{\partial \dot{m}_p}{\partial S_{\text{in}}} = -1.477 \times 10^{-7}$	5.45%
$T_{\text{c,in}} = 20.5 \pm 0.6$ [°C]	$\frac{\partial \dot{m}_p}{\partial T_{\text{c,in}}} = -8.87 \times 10^{-7}$	1.96%
$T_{\text{f,in}} = 69.5 \pm 0.25$ [°C]	$\frac{\partial \dot{m}_p}{\partial T_{\text{f,in}}} = 3.805 \times 10^{-6}$	6.29%

During operation, in spite of the spacer, the membrane does not remain flat and

at a fixed distance from the condensing plate. The membrane is pushed into the gaps in the air gap spacer due to hydraulic pressure and this reduces the effective air gap thickness, as seen in Fig. 3-3. In addition, conduction across the plastic spacer and the spacer's effect on the condensate film forming on the plate may also be important. As a result, this is one of the most difficult parameters to estimate accurately while modeling the system. The effective air gap width is smaller than the design value for these reasons and is taken to be 0.75 mm in the modeling analysis.

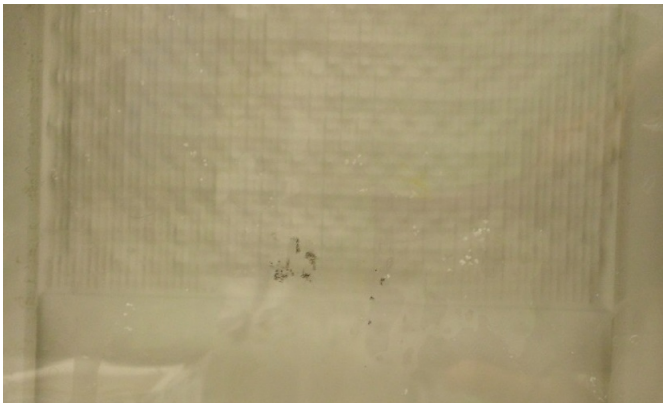

Figure 3-3: MD membrane during operation: regions of the membrane are pushed into the gaps in the mesh spacer

3.2.6 Feed, Cold Water

The feed and cold water form a closed loop flowing from large tanks that act as a thermal reservoirs that ensure relative stability in temperature values over time. The feed water flows through instrumentation that records its flow rate and temperature, into the feed module and back into the tank. The feed water temperature is controlled at a set high temperature (40-70 °C using a resistance immersion heater and a feedback controller.

The cold side tank on the other hand often needs to be cooled to maintain its temperature as it takes up the heat of condensation within the module during operation. The building cold water supply line is used for this purpose and a solenoid valve is activated to allow cold water flow into a copper tube that is immersed into

the water in the tank, whenever the tank temperature rises beyond a set value.

3.2.7 Module assembly

The apparatus is designed in a modular way with separate pieces individually defining each of the flow channels or segments. These are then held together by bolts that line all fours sides of the module. The channel sealing is an important feature for reliable operation. O-rings are used for this purpose, wherever a fluid stream needs to be confined within a given area.

The module is made up of the feed plate, MD membrane, plastic spacer, air gap mesh, metal condensing plate, and cooling channel plate (Fig. 3-4).

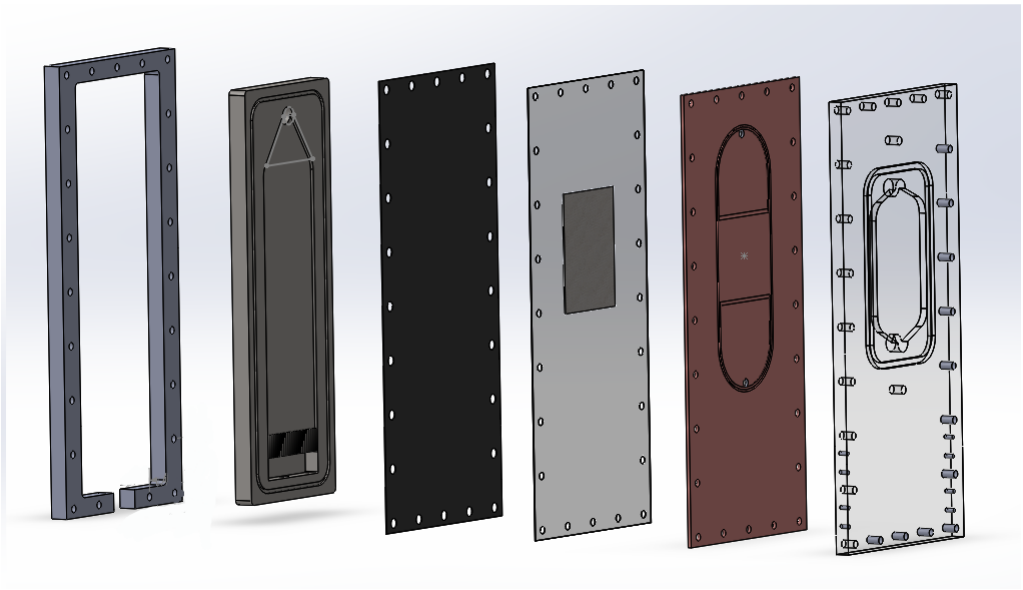

Figure 3-4: MD assembly showing individual components. Left to right: Metal flange, feed plate, MD membrane, plastic spacer with mesh spacer, condensing plate and cooling channel

Most of the pieces of the design and especially the feed plate are manufactured out of transparent polycarbonate. Polycarbonate has several useful properties that makes it an ideal choice. It has a low thermal conductivity, leading to lower heat loss from the module, which is especially important at high temperature runs. In addition, we chose a transparent material that enables visual inspection of the membrane surface

during the course of the experiment which is useful for the fouling experiments in particular. In real systems, the low cost of plastics as compared to metals is also a driver towards their use in MD installations since lower capital costs are are an important advantage of MD over other systems.

While other experimental setups of this kind have used bolts and nuts to secure the pieces of the module together, for a scaling test setup, easy removal of membrane for inspection and changing membranes is a useful feature. While all the other plates are held together by bolts, the feed plate is held down by a set of specially designed clamps that can be quickly released or fastened that help hold plate in place and press it onto the o-ring. Figure 3-5 illustrates this design in the actual experiment.

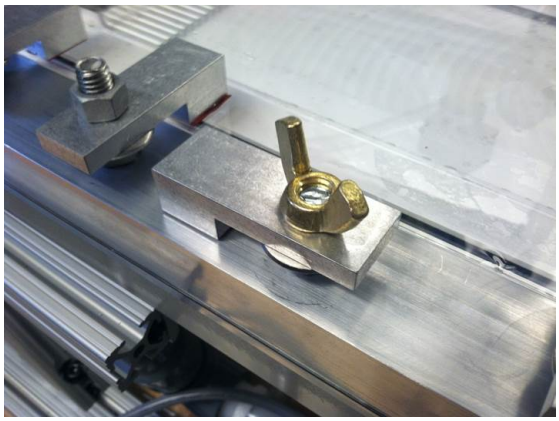

Figure 3-5: Design of quick release clamps for easy access to membrane between tests

The air gap defining plastic spacer is also made of polycarbonate, and is designed to be 1 mm thick sheet. This corresponds to the design specification of the air gap.

Several versions of the air gap mesh spacer were tried out before deciding to use the version shown in Fig. 3-6. Here there are two spacers used. The larger one is a woven mesh spacer and is placed in contact with the metal plate. In the woven air gap spacer, the 60-80% of the horizontal elements are removed to minimize interference with the film of condensate that forms on the plate. On top of this, a much thinner uniform mesh is used to reduce the stretching of the membrane material into the large gaps in the large mesh.

The condensing plate used is made of aluminum. With a high thermal conductivity

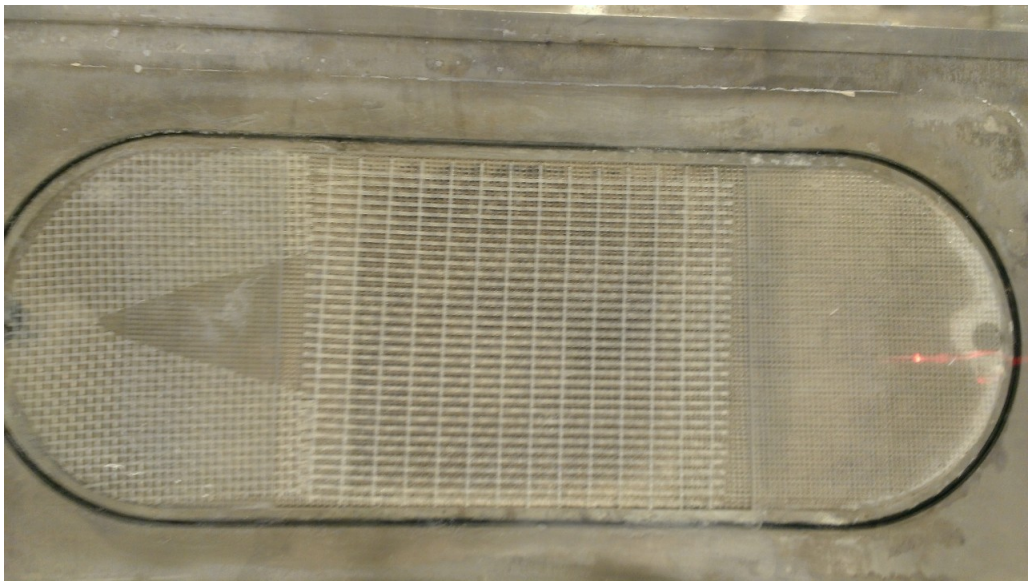

Figure 3-6: A thinner spacer stacked over the woven mesh in the air-gap

and relatively high fouling resistance due to the formation of a protective oxide layer on its surface, it is suited to an application where it is expected to be in continuous contact with pure water over long periods of time. During experiments it was found that while this is predominantly true, it is possible that some of the Al is leached out by the DI water due to its high level of purity.

The cold side channel is made of polycarbonate too. The channel depth is designed to be higher than that of the feed side so that the pressure drop is smaller and a smaller pump can be used on this side. In several real systems (AGMD, DCMD) the cold side fluid would be the feed getting preheated by the condensing permeate before it is heated to the cycle top temperature. Since this module was designed especially for fouling testing and the cold fluid temperature was expected to be kept constant during the course of the experiment and capable of being modified independently, it could be designed differently with different dimensions and flow rates as compared to the hot fluid channel. The pressure plenum and the manifold design were also eliminated in the cold side, since flow redistribution is of less importance. The aluminum plate being quite conductive, gets cooled uniformly by the flow.

The o-rings used in this setup are made of Viton material [39]. Standard o-ring

sizing charts were used to design the o-ring grooves and choose the corresponding diameter of o-ring.

3.2.8 Feed Channel

Channel length flow development

The flow velocity profile can play a critical role in influencing the extent of shear at the membrane interface and mixing within the stream. While testing for the effect of fouling inside small coupon sized modules, it is possible that the flow characteristics are very different and so the results may not be representative of real systems. To avoid this effect, the module dimensions were designed so that the active membrane area is far downstream of the channel inlet. The length of this flow developing region is designed to be ~23 d_h (hydraulic diameter) of the channel (Fig. 3-7). Under these conditions, with turbulent flow conditions, it is likely that the velocity profile will be fully developed when the flow reaches the active membrane area.

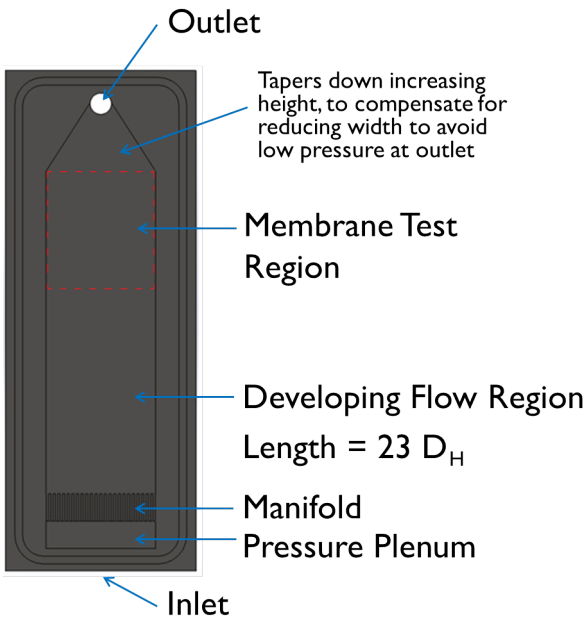

Figure 3-7: Feed channel design

Pressure plenum design

The channel inlet needs to be designed such that irrespective of the velocity profile in the inlet pipes and the placement of the inlet with respect to the channel, flow is well distributed across the entire cross section. We followed the guidelines for Uniform Flow in Dividing Manifolds in [40] to ensure that the pressure drop across the manifold outlets is an order of magnitude more than that in the water collection region. The water as it enters the module hits a wall and is forced to recirculated and fill the high pressure collection chamber before flowing out of the small and equally spaced outlets at relatively uniform speeds. Figure 3-8 illustrates the design in further detail.

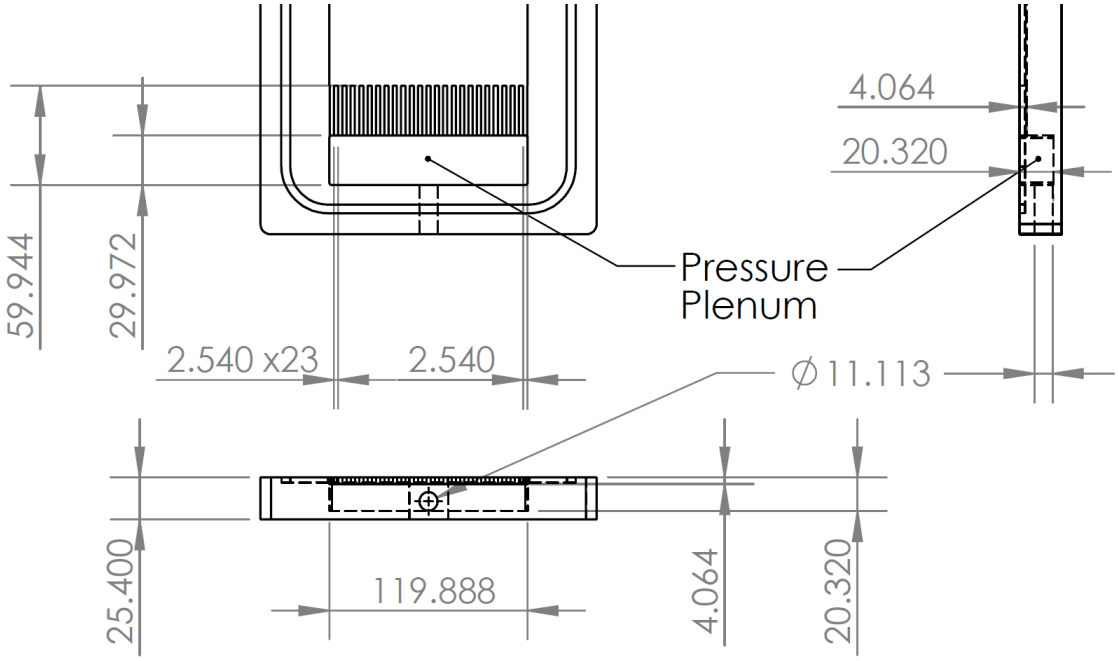

Figure 3-8: Design of inlet manifold with high pressure reservoir and outflow nozzles for uniform outflow. All dimensions are in mm

3.2.9 Membrane

The membranes used are hydrophobic Immobilon-PSQ Membranes [41], originally designed for protein binding, but have characteristics suitable for Membrane Distil-

lation. The membranes have an average pore size of 0.2 μm and maximum of 0.71 μm, and a porosity of 79.2%. They have previously been examined as the principal membrane used by Dr. Edward Summers at MIT [38].

3.2.10 Piping and Pumps

Magnetic drive pumps were chosen for both the feed [42] and cold [43] fluid loops. The magnetic drive pumps have no metallic parts that come in contact with the liquid thereby reducing chances of fouling. The piping is chosen to be flexible clear PVC tubing for the most part. Before and after the flow meter a small section of hard CPVC is used since the flow meter accuracy is guaranteed only with a long enough entrance and exit region.

3.3 Instrumentation

3.3.1 Temperature

Thermistors [44] are used for temperature measurement to achieve $\pm 0.2\,^{\circ}$C or better accuracy in the temperature readings. Thermistors were calibrated over a range of temperatures (0-80 °C) using a constant temperature bath and a Fluke high accuracy temperature probe. Pipe plug type thermistors from Omega are used for easy in-line measurements of temperature in the tubes. Care is taken to orient the tubes in such as a way that air does not collect close to the thermistor and that the air is removed during system startup.

The thermistors can act as a fin, transporting heat out of the system. This effect needs to be recognized and accounted for, in order to maintain required temperature measurement accuracy. Insulation is added to the outside of the thermistor probe and this is seen to increase the measured fluid temperature by up to 1 °C at temperatures close to 70 °C.

Temperature is measured and recorded into the computer using a DAQ board [45]. Temperature data is recorded once in every 5 seconds. The temperature needs

to maintained constant over the course of a experiment. A temperature controller is used with input from the feed tank to control the heater power input. Using this setup, it is possible to maintain the temperature to an accuracy of about $\pm 0.1\,^{\circ}\mathrm{C}$.

On the cold side, the water often needs to be actively cooled to maintain constant temperature. Using the building chilled water supply, this temperature is maintained within $\pm 0.5\,^{\circ}\mathrm{C}$. For the tests where the water is to be maintained at temperatures above room temperature, sometimes a combination of a heater element and the cooling water supply is used to maintain the temperature between a lower and upper bound, as the water tends to lose heat to the atmosphere and gain energy from the feed channel.

3.3.2 Flow Rates

Flow rates are measured using digital turbine meters with $\pm 2\%$ of full scale reading accuracy. On the feed side, the flow meter can measure between 2-20 GPM (0.126-1.26 L/s) [46] and on the cold side between 0.8-8 GPM (0.0504-0.504 L/s) [47].

3.3.3 Mass/Flux

The mass collected needs to be measured with good accuracy in order to evaluate the flux effectively. The mass values are transmitted to the computer where they are recorded along with the time-stamp. We use a mass scale with accuracy ± 0.1 g and range of 2 kg to measure the product water as it is produced [48]. The scale is connected to the computer and mass data is recorded every 5 seconds. Numerical differentiation is carried out to evaluate the flux using a center difference scheme over a total period of 180 seconds. The flux oscillates with a period equal to the oscillation in the cold side flow inlet temperature. Therefore, experiments are carried out till flux settles and completes at least one period of oscillation. The instantaneous flux values are then averaged.

3.3.4 Conductivity

The conductivity of the permeate water is measured to estimate the purity of the water produced [49]. This is important in order to know whether there is feed breakthrough through the membrane or if there is a leak into the permeate stream from either the feed or the cold water stream. On average the conductivity of the permeate water is found to be below 100 μS/cm which corresponds to a salinity less than 0.05 ppt, even when the feed salinity is close to 200 ppt. In addition to a small amount of salt transfer across the membrane, the difference in conductivity between the MD water produced and the DI water from RO system in lab (1.2-1.4 μS/cm) can also be because of the water coming in contact with aluminum on the condensing side where it can leach some of the ions, as discussed earlier.

3.4 Modeling

A numerical model was also implemented in order to understand the results from the experiment and better design fouling tests. Importantly, the model gives us a handle of the properties of the feed at the membrane interface as a function of the bulk properties and the flux through the membrane. The growth of scale on the membrane is likely to be affected most by these conditions (temperature and concentration) at the membrane interface.

The overall modeling methodology is similar to what is discussed in Section 2.2.1. Water vapor transport on the permeate side is governed by binary diffusion across the air gap as described in Summers et al. [2]. Since high salinity feed solutions are considered, the concentration polarization model on the feed side is discussed in some detail in this section.

3.4.1 Concentration Polarization

Concentration polarization was modeled using the film model of concentration polarization [50]. This model works well when the concentration boundary layer lies

well within the momentum boundary layer, therefore resulting in salt transport that is predominantly by diffusion. The convective transport of salt by the water flux through the membrane is balanced by back diffusion and convection along the membrane length direction is ignored. Integrating this equation between the bulk feed stream and the membrane gives us the commonly used film model where there is an exponential dependence of concentration polarization ratio on the ratio of flux to the mass transfer coefficient. The mass transfer coefficient comes into the picture through the thickness of the boundary layer. Since the thickness of the boundary layer would grow along the length of the module, deriving the mass transfer coefficient from a correlation for fully developed laminar or turbulent flow is an approximation.

Bhattacharjee et al. [51] discuss the detailed modeling of the concentration polarization for a multicomponent solution flowing through a rectangular feed channel for the case of nanofiltration systems. Similar detailed and more complicated numerical models may be necessary for MD systems too when more complicated feed solutions are used.

The flux is proportional to the vapor pressure difference across the membrane. On the feed side, the vapor pressure is evaluated using Eq. 3.2. The mole fraction of water at the membrane interface is evaluated using Eq. 3.3. Here the mole fraction of NaCl is multiplied by 2 since sodium chloride is a strong electrolyte and is assumed to completely dissociate into Na^+ and Cl^- ions.

$$P_{vap}\left(T_{f,m}, S_{f,m}\right) = P_{sat}\left(T_{f,m}\right) \times x_{w,m} \times \gamma_{w,m} \tag{3.2}$$

$$x_{w,m} = 1 - \left(\frac{2 \times \frac{S_{f,m}}{MW_{NaCl}}}{2 \times \frac{S_{f,m}}{MW_{NaCl}} + \frac{1000 - S_{f,m}}{MW_{H_2O}}} \right) \tag{3.3}$$

In Eq. 3.2, $\gamma_{w,m}$ refers the activity coefficient of water at the membrane interface. From Mistry et al. [52], we see that the activity coefficient and activity of water start deviating significantly from unity at salinities higher than about 90 ppt. A quadratic curve fit is therefore used to approximate the activity coefficient of water in this range.

$$\gamma_{w.m} = \begin{cases} 1, & \text{if } S_{f,m} \leq 90\,\text{ppt} \\ 2.448 \times 10^{-6}\,(S_{f,m}^2) + (0.0004262\,S_{f,m}) + 0.9809, & \text{if } S_{f,m} > 90\,\text{ppt} \end{cases} \tag{3.4}$$

The film model of concentration polarization is given by Eq. 3.5.

$$S_{f,m} = S_{f,b} \times exp\left(\frac{J}{\rho\, k_{mass}}\right) \tag{3.5}$$

k_{mass} is defined by Eq. 3.6 as:

$$k_{mass} = \frac{Sh \times D_{s,w}}{d_h} \tag{3.6}$$

The diffusivity of sodium chloride in water is a function of both concentration and temperature. An average value of diffusivity of NaCl at relatively high concentrations and T=298K is obtained from Robinson and Stokes [53] and is given by $D^{\circ}_{s,w} = 1.55 \times 10^{-9} m^2/s$. At high temperatures encountered in MD $\frac{D}{D^{\circ}} = \frac{T}{298.15}$. Therefore $D_{s,w}\,(65\,^{\circ}\text{C}) = 1.76 \times 10^{-9}\text{m}^2/\text{s}$. The mass transfer analog of Gnielinski's correlation is used to determine the Sherwood number for turbulent flow. This is an approximation since the mass transfer boundary layer is not fully developed within the small experimental channel.

3.5 Results and Discussion

3.5.1 Parametric Studies

Effect of Salinity

With an increase in salinity, flux decreases due to the decrease in vapor pressure at the liquid vapor interface formed at the membrane as described in Section 3.4.1. At low salinities this the reduction in flux is linear whereas at elevated salinities beyond about 90 ppt, the nonideal behavior of the solution results in a quicker decline in flux. Since activity coefficient of water is also included in the model calculations, nonideal

behavior alone cannot completely explain the deviation between experimental and numerical results at higher salinities in Fig. 3-10. During this experiment, rust was observed in the feed tank and the membrane was discolored. Section 3.5.2 discusses this confounding factor further and describes one possible solution to eliminate this effect. Error in the estimation of the mass transfer coefficient within the channel can also account for the deviation between experimental results and the model in Fig. 3-10 and 3-9.

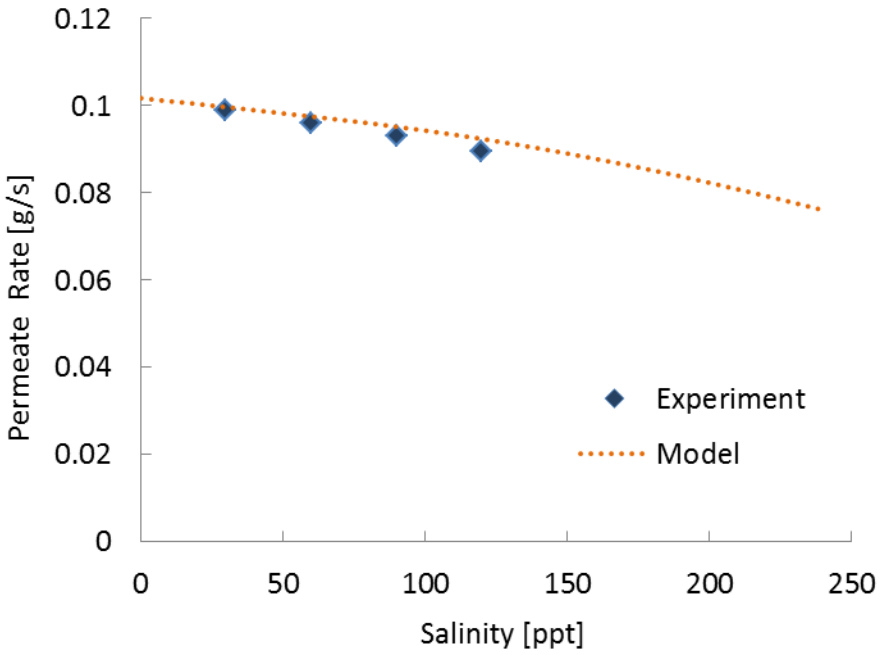

Figure 3-9: Water production rate as a function of feed inlet salinity. $T_{\mathrm{f}} = 69.5\,^{\circ}\mathrm{C}, \dot{V}_f = 0.2558\,\mathrm{L/s}$

Over the course of the tests with feed salinity ranging from 0 to 200 ppt of NaCl, the permeate water quality remained at a salinity less than 0.01 ppt.

Feed temperature variation

Water vapor pressure is an exponential function of temperature. As a result, with increases in temperature the permeate production rate also increases exponentially, as seen in Fig. 3-11 and 3-12. Figure 3-12 also compares two different orientations

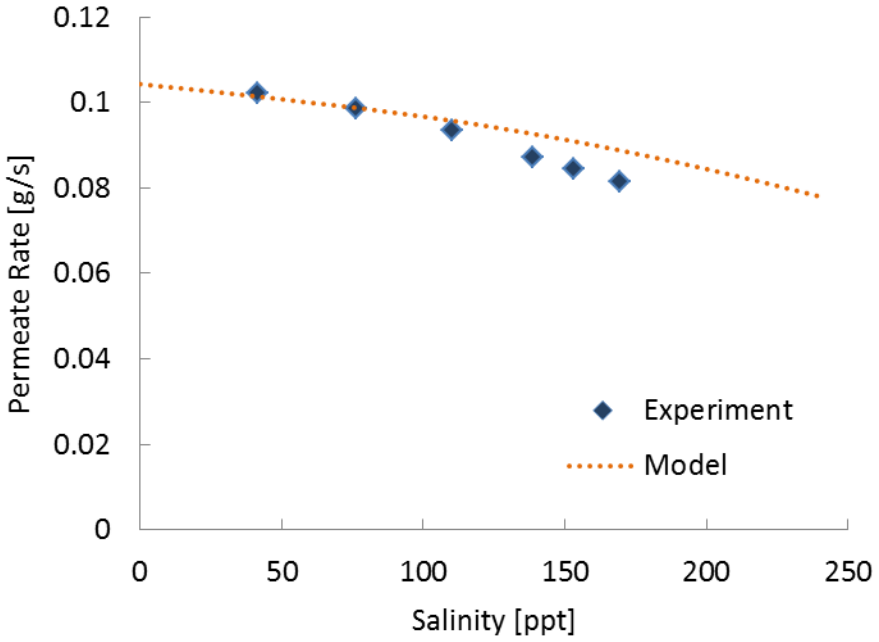

Figure 3-10: Water production rate as a function of feed inlet salinity. $T_{\mathrm{f}} = 70\,^{\circ}\mathrm{C}, \dot{V}_f = 0.252\,\mathrm{kg/s}$

of the same membrane (with different sides facing the feed at the two orientations). Small differences in flux were observed between these two cases. This can be a result of asymmetry in the membrane material with one side being the active surface and having smaller pores as compared to the other side. When the support layer of the membrane faces the feed solution, larger concentration polarization effects are expected and hence lower flux is expected. More experiments are needed to analyze this effect and understand the effect of membrane orientation on MD process.

Feed flow rate variation

The feed flow rate was varied across a large range of values covering laminar, turbulent and transition regimes. Figure 3-13 shows the experimental results for flux with changes in flow rate from 0.126 L/s to 0.284 L/s at 0.016 L/s intervals. The numerical model predictions are also plotted for comparison. At the far right, flow is turbulent, whereas everywhere else the nature of the flow cannot be known for sure. The model

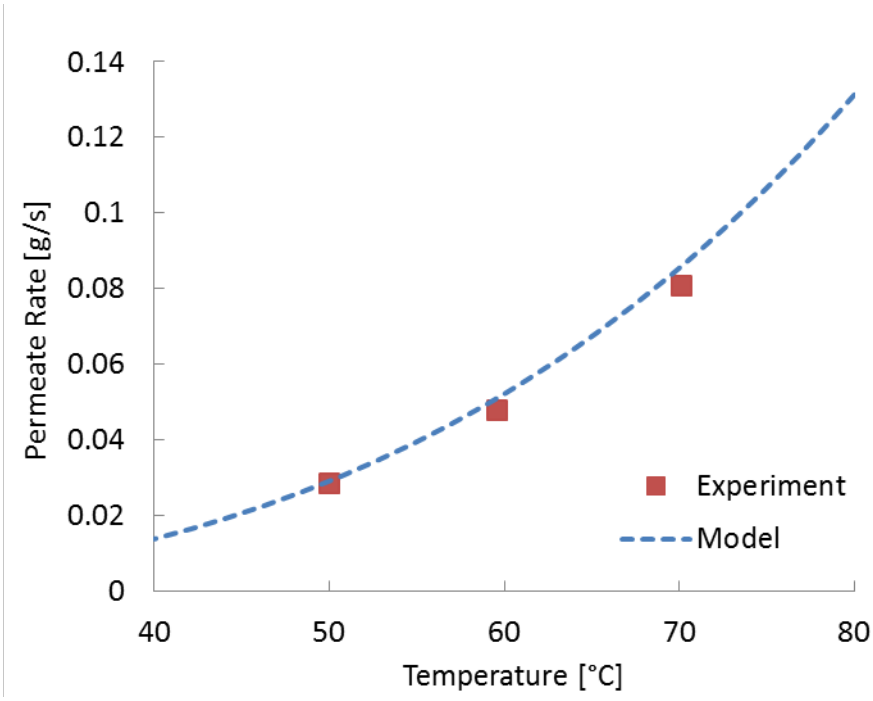

Figure 3-11: Effect of temperature on permeate production rate. $S = 191\,\text{ppt}, \dot{\text{V}}_\text{f} = 0.252\,\text{L/s}$

assumes a transition Reynolds number of 2800 which occurs at a low flow rate of about 0.076 L/s due to the low fluid viscosity at 70 °C. As a result, all the calculations were made using correlations for laminar flow in this graph.

At 44 ppt, it can also be noticed that the lines for 0 ppt and 44 ppt are nearly parallel with the 44 ppt line displaced towards the bottom. The reduction in flux is similar in both cases indicating that the extra concentration polarization factor (in the 44 ppt case) is less important and flux decline, with decreasing flow rate, is dominated by temperature polarization which is common to both cases. This can be expected since flux is an exponential function of temperature whereas it is only a linear function of concentration.

In Fig. 3-14, the lowest flow rate chosen is at 0.032 L/s. Data was acquired in steps of 0.032 L/s up to a maximum flow rate of 0.315 L/s. The overall trend is very similar to the previous case. At 0.032 L/s, there is one outlier where the flux is much lesser than what is predicted by the model, using laminar flow correlations for heat

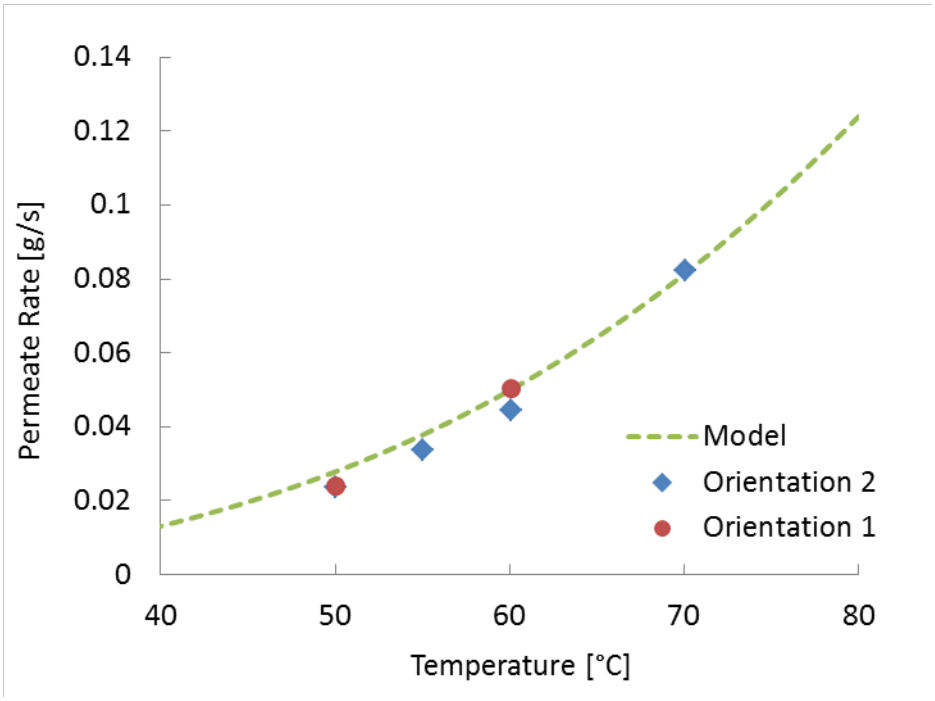

Figure 3-12: Effect of temperature on permeate production rate. $S = 198\,\text{ppt}, \dot{\text{V}}_\text{f} = 0.2678\,\text{L/s}$

and mass transfer. The reason for this deviation is discussed in Section 3.5.2.

Sufficient time was provided for the system to reach steady state before flux was recorded. Under these conditions, the maximum experimental uncertainty in flux was about 2% and hence the error bars are smaller than the size of the data markers. For the numerical model, the error associated with evaluated flux as a function of the measurement errors in model input parameters such as temperatures, flow rates and salinities was found to be about 3%. The maximum difference between model predictions and experimental data is about 10%.

3.5.2 Other Experimental Issues

Changes in effective air gap thickness

Changes in effective air gap depth during operation are undesirable since the flux is a very strong function of the air gap depth (See Section 3.2.5). While an effective air gap width of 0.75 mm considered in this study gave good predictions overall, under

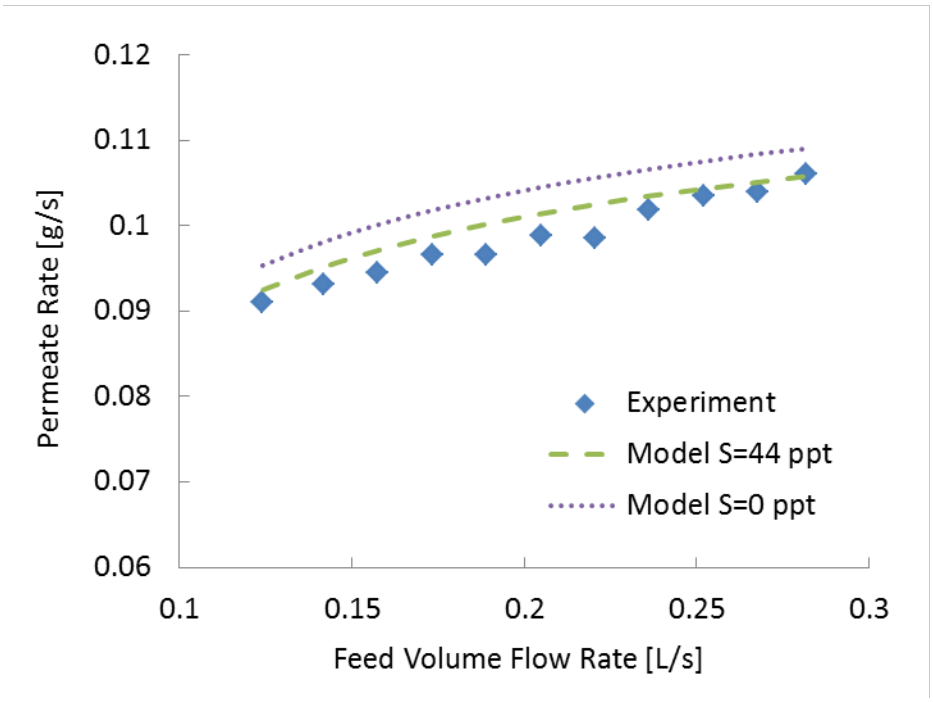

Figure 3-13: Effect of feed flow rate on flux. Model data for 0 ppt included for reference. $S = 44\,\text{ppt}, \text{T}_\text{f} = 70\,^\circ\text{C}$

certain conditions, this assumption is not valid.

The effective air gap width can be considered to be a function of the geometry of the air gap spacer and the liquid pressure inside the feed channel. During any given experiment, while the former cannot change, the pressure in the feed tank can, with changes in system operating conditions. The most straightforward way in which this is can happen is with changes in the feed flow rate. The feed flow rate was controlled with the help one or both valves located just before and just after the feed channel.

In Fig. 3-13, to reduce the flow rate up to 0.126 L/s, only the valve before the module was activated. When this valve is closed, the total flow rate reduces and since the loss coefficient in the section following the module remains constant, there is a corresponding reduction in hydraulic pressure in the channel. An extreme case of this is what happened in the 0.032 L/s test illustrated in Fig. 3-14. At this very low flow rate, since the module is at an elevated position compared to feed tank, the hydrostatic pressure in the feed drops below P_{atm} resulting in the membrane bulging

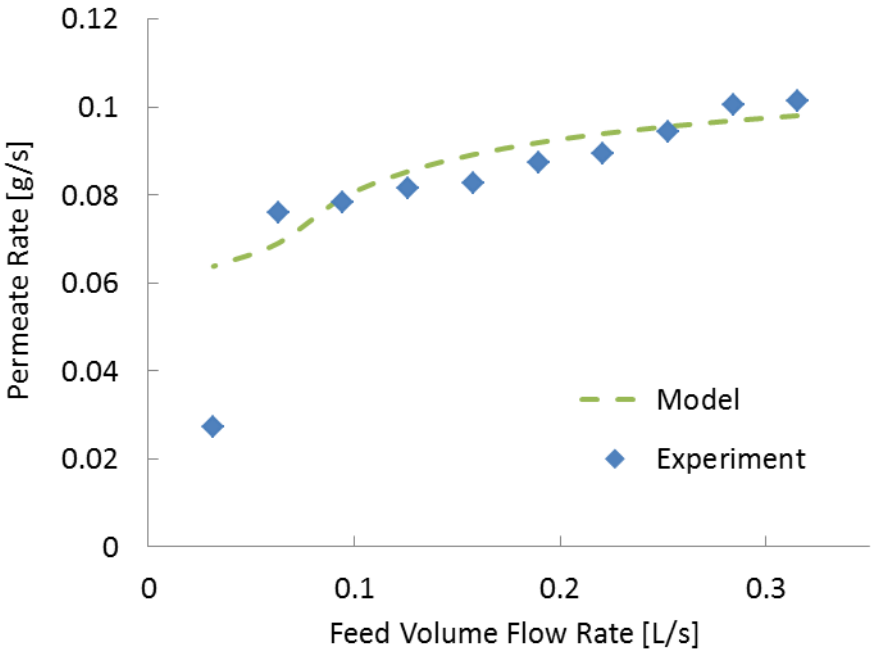

Figure 3-14: Effect of flow rate on flux. Feed flow rate varied from 0.032 L/s to 0.315 L/s. $S = 70\,\text{ppt}, \text{T}_\text{f} = 69.5\,^\circ\text{C}$

out into the feed channel rather than being pressed against the spacer. This leads to an increase in effective air gap thickness and can explain the large reduction in flux observed.

While conducting the experiments for the data reported in Fig. 3-15 and 3-16, both valves were used at low flow rates to avoid this condition. Therefore, the membrane was not allowed to bulge back into the feed channel and was always pressed against the spacer. In Fig. 3-15 and 3-16, at each temperature of 40,50,60 and 70 °C, experiments were conducted at 0.063 L/s, 0.095 L/s, 0.189 L/s and 0.252 L/s. Larger deviations are still observed at 0.063 L/s, 0.095 L/s where both valves were used. The issue in this case is that, though the membrane does not bulge out into the feed channel, the pressure inside the feed channel is variable and therefore in some cases, the gap thickness could be smaller at the lower flow rates. Since flux is a much stronger function of gap thickness than of flow rates, this acts as a confounding factor in understanding these graphs. The experiments were started off at highest temperature

and flow rate. The flow rate was first reduced in steps up to 0.063 L/s, at which the point the temperature was stepped down to 60 °C and flow rates were increased up to 0.252 L/s and so on. As a result, changes in gap thickness can persist between experiments too.

Since the pressure inside the channel is neither directly measured, nor easily inferred (variable valve openings), the only solution would be to work over a smaller range of flow rates, closer to 0.252 L/s, where this effect is less pronounced. If lower flow rates need to be studied, it is advisable not to compare results form multiple flow rate cases. Instead, at a fixed flow rate (∼0.063 L/s), the effects of temperature and salinity can be observed. For example, in the above experiments, the flux observed in the 100 ppt experiment was always lower than that observed in the 2 ppt experiment at the same value of feed temperature and flow rate.

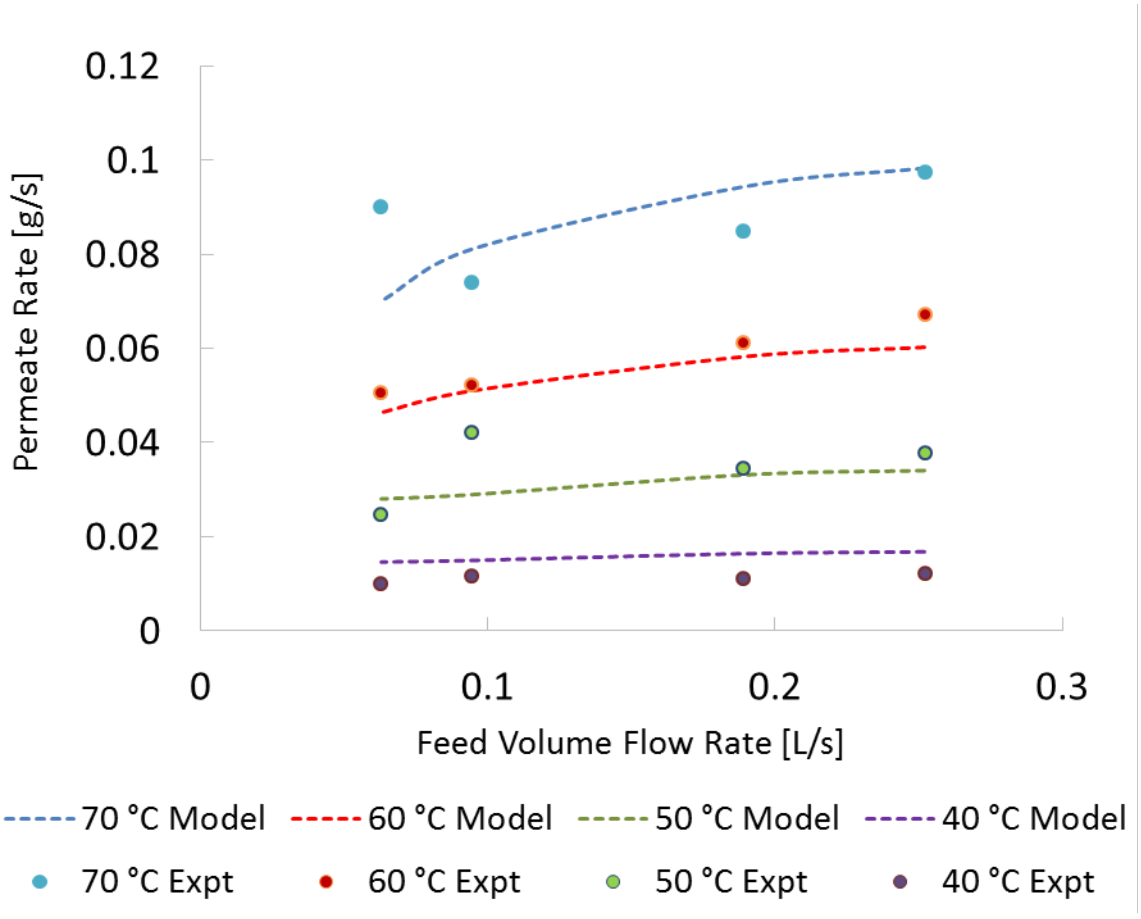

Figure 3-15: Flux as a function of temperature and flow rate. S=100 ppt

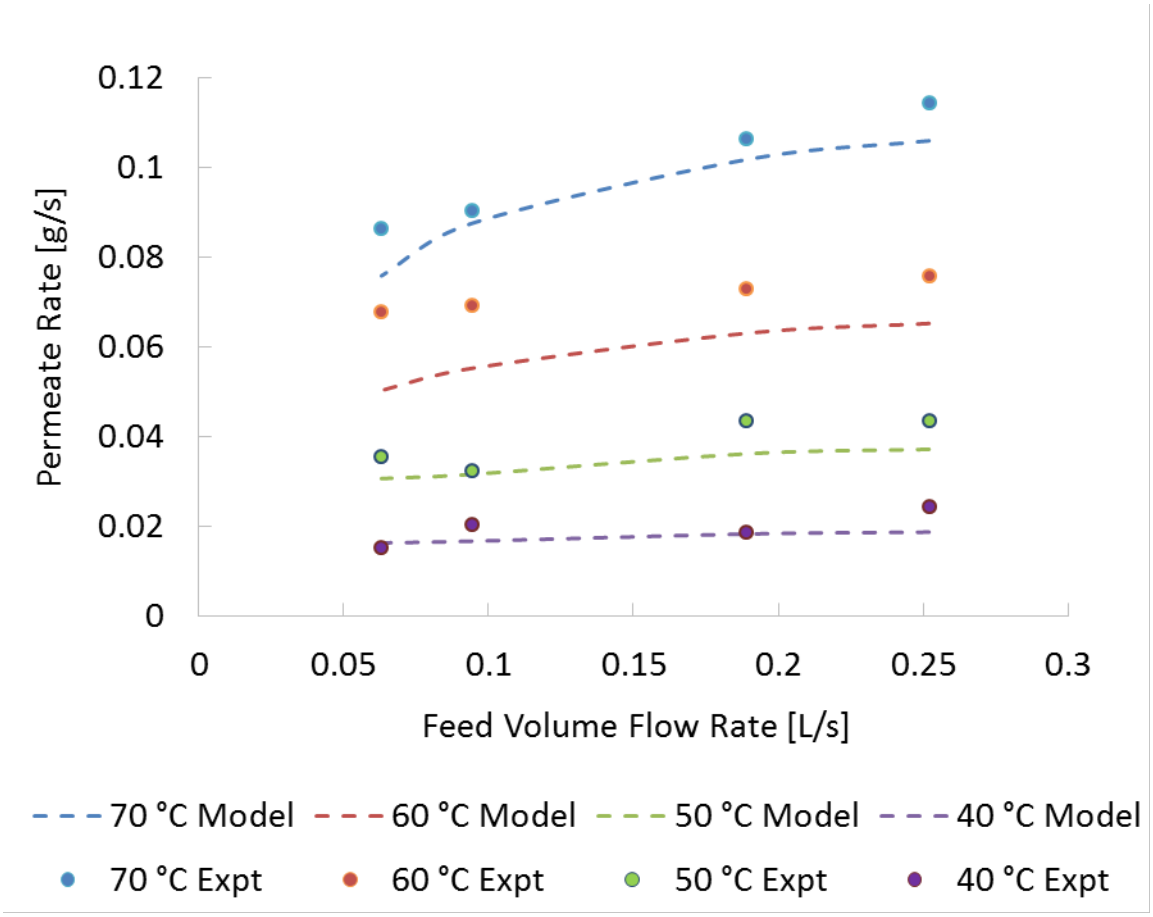

Figure 3-16: Flux as a function of temperature and flow rate. S=2 ppt

Heater rusting

While care was taken to choose pumps and pipe fittings that were fouling resistant and stable at high temperatures, the heater element itself, though made of stainless steel was prone to rusting and this contaminates the feed stream. It was noticed that under these conditions, the membrane tended to get fouled more readily, with flux decline and salt water breakthrough also observed in some experiments. Figure 3-17 shows the existence of brown rust along with $CaSO_4$ precipitate during an experiment with supersaturated calcium sulphate feed. Figure 3-18 shows that the membrane was discolored at the end of the high salinity test shown in Fig. 3-10.

In order to avoid this, the feed tank can be redesigned to physically separate the

Figure 3-17: Rust seen on heater element in $CaSO_4$ supersaturation experiments

heater element from the feed solution. For this purpose, a batch tank liner bag made of polypropylene has been used. This bag is filled inside with pure water or tap water which is heated by the heater. The flow around the bag induced by the outflow and inflow of feed in the main tank enables good heat transfer from the large surface area of the bag to the actual feed solution. A cylindrical wire structure is also used for preventing direct contact of the bag with the heater which can cause the bag to melt. Figure 3-19 illustrates this apparatus. This contraption was used successfully to prevent fouling.

3.6 Conclusions

The design methodology and steps in the design of an air-gap membrane distillation lab scale experimental setup were presented in detail. In particular the design features essential for an experimental setup used to evaluate scaling and fouling in MD are considered.

Some unique challenges that are encountered in this experimental procedure such as changes in air gap width, difficulty in replacing membranes, heater scaling etc. are discussed and innovative design solutions are presented where applicable.

Figure 3-18: Membrane used for experiment (Fig. 3-10) showing discoloration

The experimental setup was used to study the purification of sodium chloride solutions at high concentrations. Some important results from this study include:

1. Permeate salinity maintained below 0.05 ppt (0.005%) after several days of operation with highly saline 200 ppt (20%) sodium chloride feed solution. MD is suitable for high salinity feed treatment

2. 20% reduction in flux with a 4.25x increase in salinity of feed stream. Initially, flux declines linearly with salinity. Faster decline is observed beyond 100 ppt due to deviation from ideal solution behavior

3. Raolts law combined with the film model of concentration polarization can explain the flux decline observed for NaCl feed solutions. The maximum percentage difference between experimental measurements and numerical data is 10%, when the air gap thickness is maintained relatively constant. This concentration polarization model can be used as a baseline for further fouling tests to find out further reductions in flux caused by membrane fouling.

4. Membrane orientation may affect the extent of polarization for asymmetric membranes. This effect needs to be investigated further under high temperature and salinity conditions where it becomes discernible.

5. The difficulty associated with experimentally varying feed flow rate as an in-

Figure 3-19: Heater separated from feed tank using a plastic bag

dependent parameter without affecting the more sensitive air gap thickness is discussed.

Chapter 4

Effect of Module Inclination Angle on Air Gap Membrane Distillation Flux

David E. M. Warsinger contributed to this chapter.

Abstract

Air gap membrane distillation (AGMD) experiments were performed with varied temperature and varied module inclination angles to characterize the effect of module inclination angle on permeate production. While AGMD is potentially one of the most energy efficient membrane distillation configurations, transport resistances in the air gap typically dominate, often dictating the flux performance of a system. Tilting the module away from vertical offers the opportunity to manipulate the condensate layer and its associated thermal resistance. In this chapter, we report experiments on varying module tilt angle performed with a flat plate AGMD setup under fully characterized heat and mass transfer conditions. Numerical modeling is also performed to better understand the experimental results. The tests indicated that the AGMD system behaves as a permeate gap, or flooded membrane distillation system for declined and extremely inclined positions. A key finding relevant to all AGMD systems is that at highly negative tilt angles (more than 30 degrees), condensate may fall onto the membrane causing thermal bridging and increased permeate production. Near vertical and positive tilt angles (<15 degrees from vertical) show no significant effect of module tilt on performance, in line with model predictions.

4.1 Introduction

Membrane distillation (MD) is an emerging thermally-powered desalination technology with unique advantages at small scales, and potential to reach superior efficiencies compared to existing desalination technologies. In an MD system, a hot, saline solution with a high vapor pressure flows across a hydrophobic membrane which selectively allows water vapor to pass through but not liquid water or dissolved salts. Pure water diffuses through the membrane and is condensed and collected on the other side. Due to its scalability and low maintenance, most applications to date for this emerging technology have been for small installations, some driven by solar thermal power [54]. Recent papers have suggested that MD can theoretically provide superior efficiencies to all other thermal desalination technologies, including Multi-Stage Flash (MSF) and Multi-Effect Distillation (MED) [55, 56], although actual test results have shown more modest thermal performance [57]. Several configurations have been designed for MD, including the most commonly, Direct Contact Membrane Distillation (DCMD) and Air Gap Membrane Distillation (AGMD), as well as Vacuum Membrane Distillation (VCMD), and Sweeping Gas Membrane Distillation (SGMD) [20]. Of these configurations, it has been shown that AGMD has higher potential for superior thermal efficiencies [2].

AGMD includes a saline feed, a hydrophobic membrane, an air gap behind the membrane, and a condensing surface beyond the air gap. Various configurations have been designed, including flat sheet designs, a tubular configuration with concentric cylinders, hollow fiber modules and spiral wound modules [20]. This study examines the effect of varying the tilt angle of AGMD modules, which is primarily applicable to flat plate configurations, but also to tubular and spiral wound systems. Flat plate systems are among the most common due to their ease of manufacturing and assembly, and are used in experimental systems as well as commercial modules such as those produced by MEMSYS [58].

In AGMD systems with small air gaps, an important phenomenon that can occur during operation is flooding and associated thermal bridging. Flooding occurs when

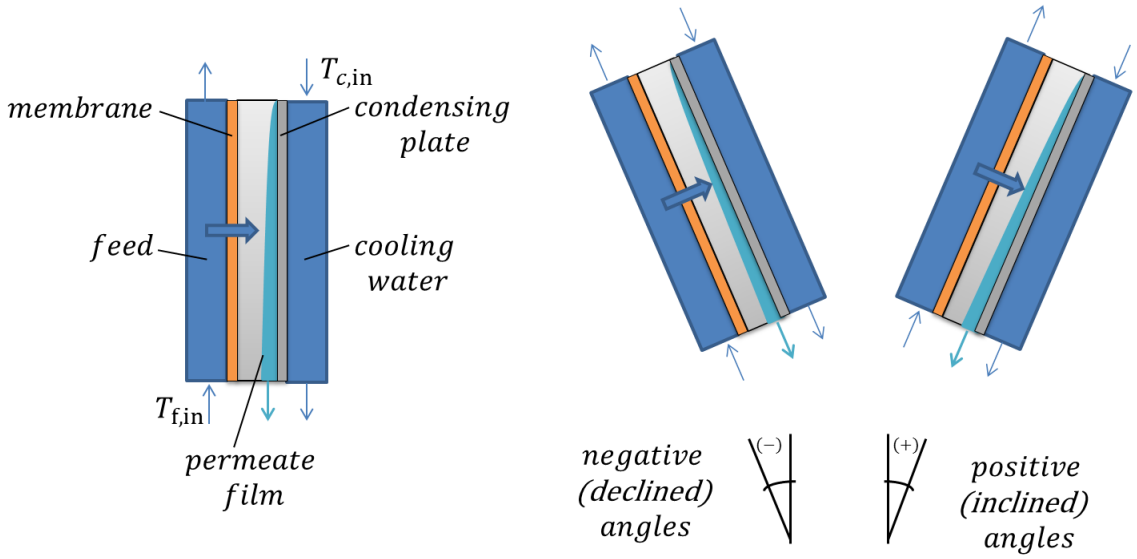

Figure 4-1: AGMD at varied angles

the permeate production rate exceeds the rate of condensate removal from the air gap. This effect reduces mass transfer resistance, tending to increase permeate production rate, but it also increases heat loss from and temperature polarization in the feed channel as heat is conducted directly through the water from the membrane to the cooling plate. Thermal bridging may also occur at small, localized regions at which water falls from the condenser onto the membrane surface for declined tilt angles, if local bridging of the membrane and condensation plate occurs. As this phenomenon is unsteady and localized, it cannot be readily modeled in the generic model.

Module tilt angle has been studied in many condensation technologies. While the vertical module orientation has been the norm in AGMD studies [59], horizontal module orientation has also been used in some cases [60], which we define here as angles approaching positive 90° from vertical as seen in Fig. 4-1. While relatively unimportant in other configurations such as DCMD, where tilt angle only has hydrostatic effects, the module tilt angle affects droplet flow and film thickness on the condenser surface in AGMD systems. The literature generally lacks experiments at other angles, although 45 degrees has been examined for DCMD, not AGMD, configurations in experiments using bubbles to encourage turbulence [61]. To the authors'

knowledge, the present study is the first detailed experimental and theoretical analysis of the effect and optimization of tilt angle on an AGMD process, and the first to examine declined angles for AGMD.

4.2 Apparatus Design

The AGMD apparatus used is the one whose construction and design were discussed in detail in Chapter 3. The module can be oriented at both positive and negative angles from the vertical as shown in Fig. 4-1. The positive angles are more stable and larger positive angles can be achieved (up to 90° possible), whereas on the negative side, the maximum angle that was tested was −60°.

To analyze the effect of module tilt angle, experiments were performed on the AGMD test bed at various inclination angles under different combinations of feed and cold side temperature conditions and with different air gap spacer meshes [62].

4.3 Numerical Modeling

4.3.1 Modeling Methods and Feed Channel Modeling

The theoretical performance of the AGMD system at varied angles is estimated using numerical modeling techniques with Engineering Equation Solver (EES) [23], which is an iterative equation solver with several thermodynamic property functions built into it. A one-dimensional modeling approach is followed in which the temperatures and flow rates vary along the length of the module. The width of the module is assumed to be long so that the effect of the walls is negligible and properties are constant along this direction. In the depth direction, the boundary layers and associated resistances are taken into account, and the difference between the temperature and concentration for the bulk stream and at the membrane interface is evaluated using suitable heat and mass transfer coefficients.

The primary modeling calculations involve mass and energy conservation equations applied to each of the module sections: the feed channel, the air gap, and the

coolant channel (Figure 4-2). Each section is coupled with suitable transport equations. A detailed description of the overall modeling methodology applied for the case of vertical module orientation is given by Summers et al. [2]. The heat and mass transfer coefficients are determined through the Nusselt and Sherwood numbers evaluated within each stream. The equations are solved using EES, and the number of computational cells was progressively increased to 120, by which point the results were seen to be grid independent.

Some important features of the model relevant to variations in flux associated with module orientation are discussed below.

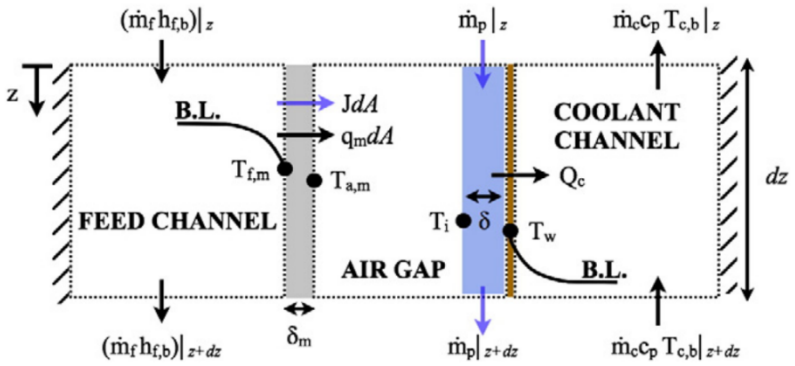

Figure 4-2: Computational cell of the AGMD model from [2].

The mass of water vapor transferred through the membrane is given by the membrane characteristic equation (Eq. 4.1) and depends on the water vapor pressure on either side of the membrane. The mass flow rate in the feed stream reduces correspondingly.

$$J = B \times (P_{\text{vap,f,m}} - P_{\text{vap,a,m}}) \tag{4.1}$$

Here J is the permeate flux, B is the membrane permeability, $P_{\text{vap,f,m}}$ is the vapor pressure on the feed side surface of the membrane, and $P_{\text{vap,a,m}}$ is the vapor pressure on the air gap side surface of the membrane.

4.3.2 Air Gap and Condensing Channel Modeling

The air gap modeling is especially important since the transport resistances in this region significantly affect the AGMD module performance. Varying the tilt angle of the module can affect the process only through physical changes in this region. Typically, a spacer mesh is placed in this region to prevent the flexible membrane from collapsing onto the condensation surface. Like most other numerical models of the AGMD module, the spacer is not explicitly considered and a free air gap is modeled.

During operation, part of the membrane is pressed down into the gaps in the mesh and the effective air gap depth is reduced. For modeling purposes though, the membrane is considered to be flat for simplicity. No condensation or heat transfer through the polypropylene mesh spacer is considered. The effective depth of the air gap is taken at a value lower than the design value (1 mm) in order to account for these effects. The water vapor flux entering the air gap diffuses through the air layer to reach the film and condense. Since the air gap is thin, any convection effects are ignored.

The flux through the membrane is a function of the vapor fraction at the interface on the air gap side. The vapor diffuses to the water interface from this interface. The diffusion is governed by binary mass diffusion as described in Lienhard and Lienhard [30] as:

$$\frac{J_m}{M_w} = \frac{c_a D_{w-a}}{d_{\text{gap}} - \delta} \ln\left(1 + \frac{x_i - x_{a,m}}{x_{a,m} - 1}\right) \tag{4.2}$$

Here, J_m is the flux through the membrane, M_w is the molecular weight of water, ca is the concentration of air, D_{w-a} is the diffusivity of water in air, d_{gap} is the air gap width, ξ is the water mole fraction at the liquid-vapor interface, and $x_{a,m}$ is the water mole fraction at the membrane interface. The thickness of the air gap increases as more liquid condenses into it. By mass conservation, assuming no shear at the liquid-air interface, the rate of growth of the film can be evaluated as

$$\delta_{i+1}^3 = \delta_i^3 + \frac{3\, J_i\, \nu_{f,i}\, dA}{g\, cos\theta\, (\rho_f - \rho_g)\, w} \tag{4.3}$$

where δ_i is the condensation film thickness, dA is the differential of area, ν_f is the fluid kinematic viscosity, g is the gravitational constant, ρ_f is the fluid density, ρ_g is the combined air and water vapor density, and w is the width [63].

Note that the denominator here has $\cos(\theta)$ to account for the angle of inclination. When the module is vertical, $\theta = 0°$. The formula is used for angles as high as 85°, since the evaluated film thickness is still smaller than the air gap thickness. The heat of condensation is conducted across the film, through the aluminum wall, and into the coolant liquid.

4.3.3 Modeling Inputs

The numerical model takes the following inputs: geometry of the experimental setup including the length, width, and depth of each of the channels; hot water flow rate and temperature as it enters the module; and cold water flow rate and temperature at module inlet.

4.3.4 Effect of Module Tilt Angle

Figure 4-3 shows the effect of tilt angle on flux in the model. The permeate production rate at a given module inclination is normalized with respect to the flux at vertical orientation and the ratio is plotted with respect to inclination angle. With all other conditions remaining the same, the thickness of the condensate film is affected by angle (Eq. 4.3). With a thicker film, the effective diffusion length ($d_{\text{gap}} - \delta$) for water vapor is reduced, and hence the flux increases (Eq. 4.2). This effect is independent of whether the module tilt angle is in the positive or negative direction.

An increase of around 4% is possible at very large module tilt angles as a result of the film becoming thicker. Figure 4-3 shows that this increase is higher for cases with lower cold side temperatures since viscosity of the film is higher and hence the film rolls off the surface slower. This small increase does not include the effects of

thermal bridging or flooding.

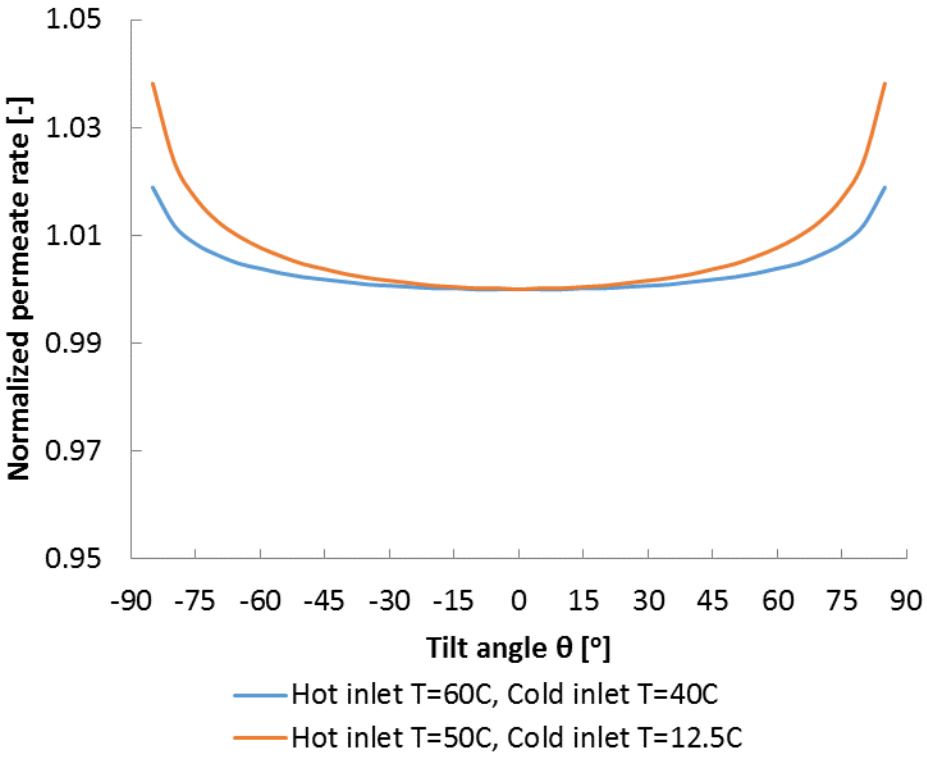

Figure 4-3: Effect of module tilt angle on flux predicted by model

4.4 Methodology

4.4.1 Experimental Methodology

The measured permeate production rates, adjusted for temperature variability, are presented. The hot side inlet and cold side inlet temperatures were set and maintained using temperature controllers during experiment operation. The hot side temperature in this experiment varies by ±0.2 °C over the course of an experiment; and on the cold side, the temperature controller, which actuates a coolant flow valve, achieves temperature control of ±0.5 °C around the set-point temperature. Between experiments at different angles, the average inlet temperatures of the streams can change. The difference in average temperature on the feed side is at most 0.4 °C and on the

cold side it is at most 1 °C. While Fig. 5 shows the relatively minute effect of tilt angle on flux, the stream temperatures have a much larger influence on flux. This is especially true because vapor pressure, which is the driving force for MD mass transfer, is an exponential function of temperature. In order to separate the effect of angle, the variability caused by small changes in average inlet temperatures must be identified and removed.

Using the corresponding average inlet temperature and flow rate conditions at each of the tilt angles, flux is estimated using the EES model for a vertical module operating under those conditions. The measured flux for the AGMD experimental system at vertical orientation was between 150-250 L/m^2 day depending on the feed flow conditions and the type and thickness of the air gap spacer used. The measured permeate production rates are scaled by multiplying by vertical module flux obtained from EES at the same temperature conditions divided by the experimentally obtained flux at 0° tilt angle. The scaled experimental fluxes are then each divided by scaled flux at 0°. The ratio obtained is called the normalized permeate rate and will have a value of unity at 0° tilt angle. At other tilt angles, the deviation from unity would indicate the relative change in flux that results from tilting the apparatus if other conditions were to remain exactly the same.

4.4.2 Uncertainty Quantification

Uncertainty analysis was performed within the EES code to account for uncertainties in numerically predicted flux as a result of uncertainties in measured temperatures and flow rates of the hot and cold streams. The overall uncertainty in flux was generally dominated by temperature variations. While the hot side temperature has a larger impact on flux, the absolute uncertainty in cold side temperature is higher, so that both affect overall uncertainty. The uncertainty in actual temperature measurements was estimated conservatively as the standard deviation in temperature recorded during the experiment plus the maximum measurement uncertainty of ±0.2 °C for the thermistors used.

Experimentally, the flux is determined over a period of 10-15 minutes by sub-

tracting the final water mass from the initial water mass and dividing by the total elapsed time. Each measurement is carried out at time intervals of about 5 seconds by the data acquisition system. Hence a time measurement uncertainty of 10 seconds is considered. A conservative time error was used to account for variability in permeate drop collection from the apparatus. The measurement uncertainty on the mass scale is ±0.1 g. In order to account for both the initial and final readings, an uncertainty of ±0.2 g is considered for the total water mass collected.

4.5 Experimental Results

4.5.1 Effect of Angle on Permeate Flux

The experiments and modeling showed a minimal effect for small inclination angles on permeate flux. Very large angles, however, did produce a substantial increase in permeate production rate. This result is further supported by theoretical analysis of the relationship between the film thickness δ and the mass transfer resistance in the air gap and flux. The main parameter of interest is the permeate production rate; as the end product, permeate flux indicates the performance of the fixed size AGMD system with fixed top and bottom temperatures of the system. While energy efficiency of the system is also important, our apparatus does not incorporate energy recovery at the condenser, and is not intended for energy consumption studies.

Figure 4-4 shows the normalized permeate flow rate vs. tilt angle. The normalized permeate flow rate is the permeate flow rate for the given angle normalized for temperature changes and divided by the permeate flow rate for vertical module orientation (0°). In Fig. 4-4, MD was performed at moderate temperatures with a high temperature difference, ΔT, between condensate and feed streams and a very low condensate temperature. Permeate flux remained relatively stable but increased at extreme angles, both for negative and positive positions. The large ΔT and very low cold side temperature caused a relatively high permeate flux. The data show a substantial jump in permeate flux at 85°, which can be attributed to air gap flooding.

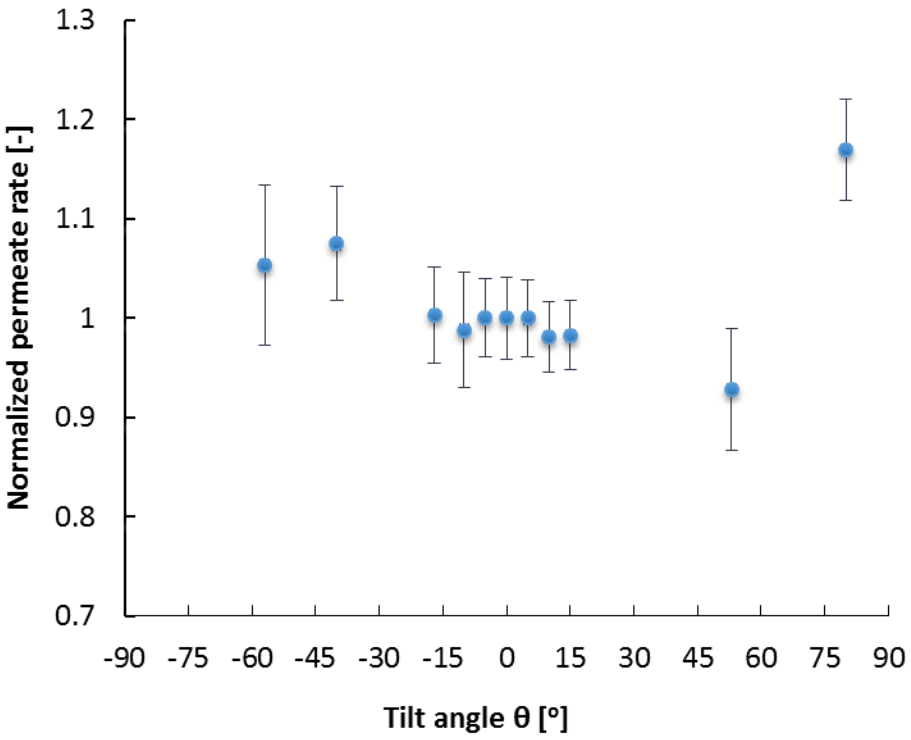

Figure 4-4: Effect of module tilt angle on permeate production: $T_{\mathrm{f,in}} = 50\,^{\circ}\mathrm{C}$, $T_{\mathrm{c,in}} = 12.5\,^{\circ}\mathrm{C}$

For this nearly horizontal case, the role of gravity in draining the film is substantially diminished (cf. Eq. 3). Additionally, for the low condenser temperature of 12.5 °C, the viscosity of liquid water is roughly twice the value in later trials at 30 °C, also contributing somewhat to a thicker condensate film.

Figure 4-5, for a trial at significantly higher temperature than Fig. 4-4, shows that angle played a small role in positive and moderately negative angles, but that flux increased significantly at very large negative angles. This may be indicative of thermal bridging at relatively small negative angles such as $-30°$, rather than flooding, and a tendency to flood as the module tilt angle further increases and approaches $-60°$.

Since it is almost universally observed that thermal bridging or other effects of module tilt angle variation are effectively absent at low tilt angles, subsequent trials reduced the number of angles considered in the low angle range.

To further investigate the hypotheses of thermal bridging and flooding, additional

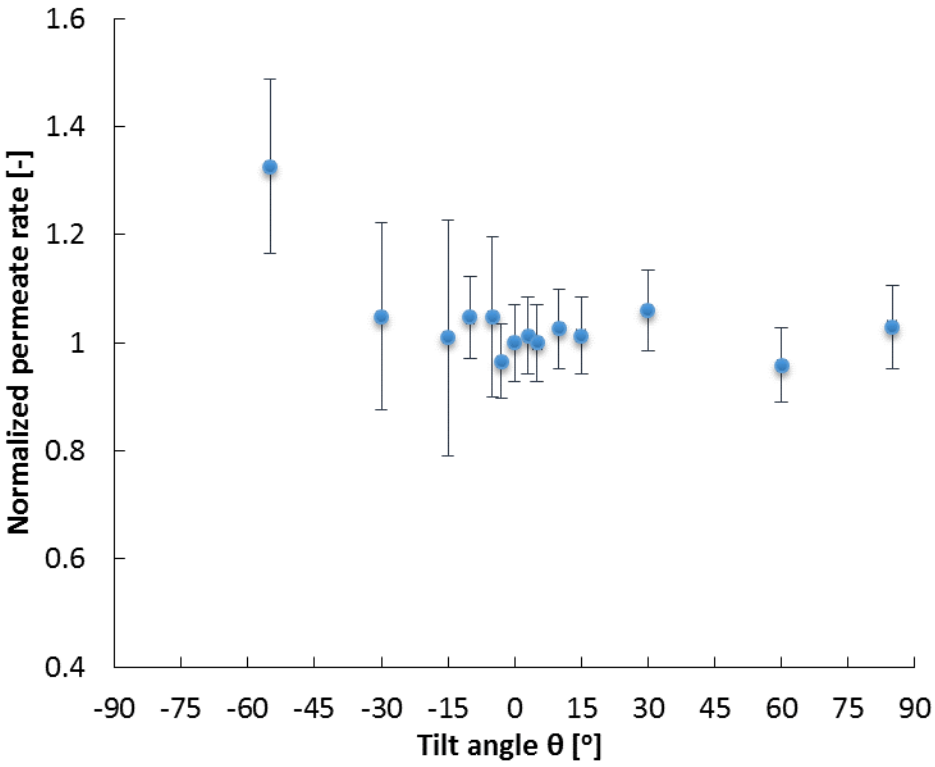

Figure 4-5: Effect of module tilt angle on permeate production: $T_{\mathrm{f,in}} = 60\,^{\circ}\mathrm{C}$, $T_{\mathrm{c,in}} = 40\,^{\circ}\mathrm{C}$.

trials were performed for a smaller effective air gap thickness two thirds the original thickness, using only one spacer mesh instead of two (Fig. 4-6 and 4-7). While the absolute value of permeate production rate was higher for these cases due to the reduction in effective air gap size and a corresponding decrease in diffusion length for water vapor, the relative effect of tilt angle on flux remains similar. At small negative angle and even at large positive angles, the flux remains constant. At $-60°$, flux increases significantly. In some cases, the effect of thermal bridging can be discerned at angles as low as $-30°$. Thus, these observations suggest that changes in effective air gap thickness do not have a major impact on the induction of thermal bridging effects at various tilt angles in AGMD. Notably, the higher temperature trial experienced relatively significant thermal bridging starting at an angle of only $-30°$, indicating a temperature dependence on risk for thermal bridging.

An additional trial was performed with hydrostatically forced flooding, where

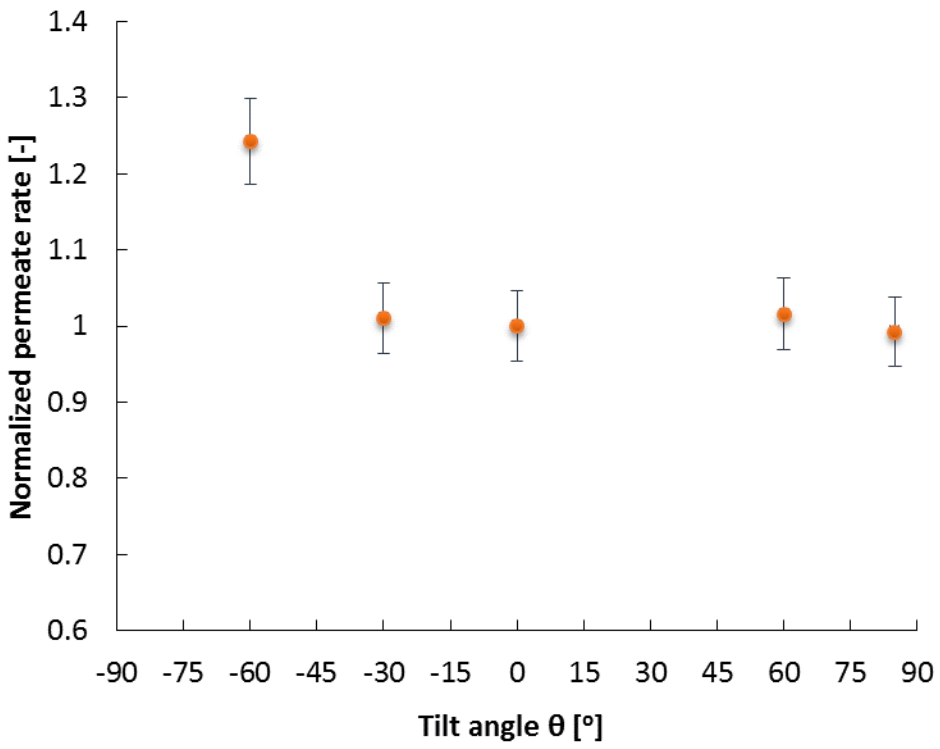

Figure 4-6: Effect of module tilt angle on permeate production: Smaller air gap. $T_{\mathrm{f,in}}$ = 50 °C, $T_{\mathrm{c,in}}$ = 20 °C.

the permeate outlet was at a larger height than some parts of the module, thereby partial filling the air gap with liquid water. At low negative angles ($\sim -30\,^{\circ}$C), partial flooding begins occurring; whereas when the angle is decreased further ($\sim -60\,^{\circ}$C), almost the entire active membrane area is beneath the outlet and hence filled with water. Identical experiments were also performed where care was taken to avoid hydrostatically forced flooding over the active membrane area even at extreme negative angles. The results showed that forced flooding, where the entire air gap is filled with liquid water produced significantly higher permeate flux (Fig. 4-8). In the tests for which forced flooding was avoided, one can see that even at -30°, the permeate production rate does not change relative to the vertical baseline. Only at higher negative angles we see an increase in relative flux, but the extent of increase is smaller than the case of forced flooding, pointing to the possibility of water falling back onto the membrane from the condensation plate and related local thermal bridging.

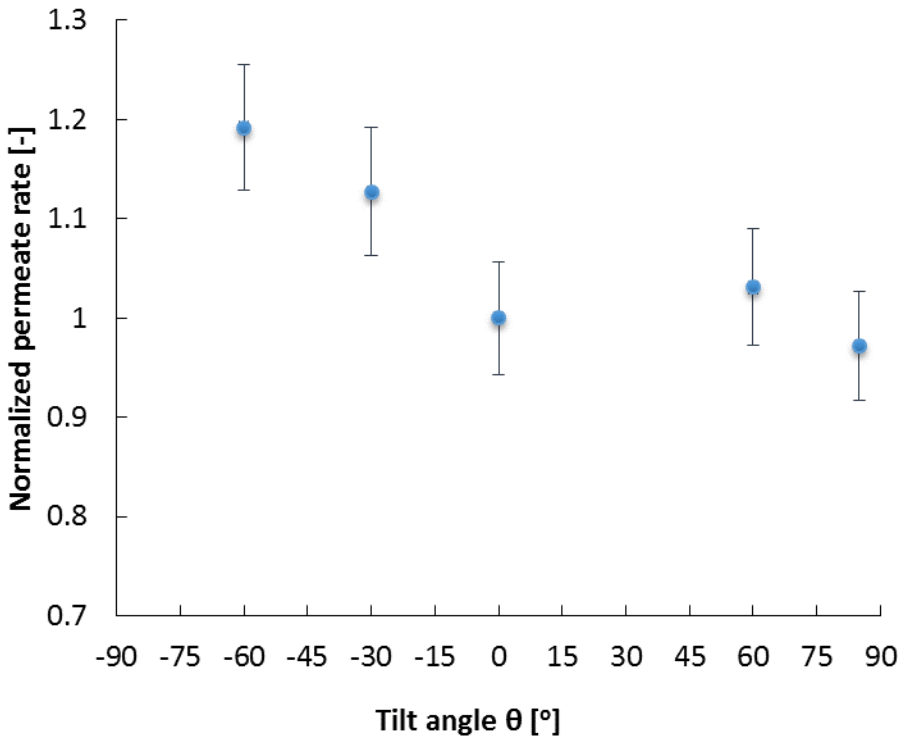

Figure 4-7: Effect of module tilt angle on permeate production: Smaller air gap. $T_{\mathrm{f,in}}$ = 60 °C, $T_{\mathrm{c,in}}$ = 40 °C.

This further demonstrates that both flooding and thermal bridging are possibilities in AGMD at high inclinations and that the relative increase in flux is affected greatly by the extent of thermal bridging.

4.5.2 Thermal Bridging Hypothesis

The thermal bridging may occur if fluid falls from the condensing plate onto the membrane itself, forming a liquid bridge across the local air gap. This phenomenon is not captured by the numerical model. Thermal bridging is particularly likely in the case of negative tilt angles and hence the experimental flux results are asymmetric about the 0° orientation. As the mass transfer resistance is dominated by the air gap width, this phenomena should be easily observed by an increase in permeate flux at declined angles. Our initial hypothesis was that bridging could occur even at small negative angles. In the experimental data, however, we see no such change in

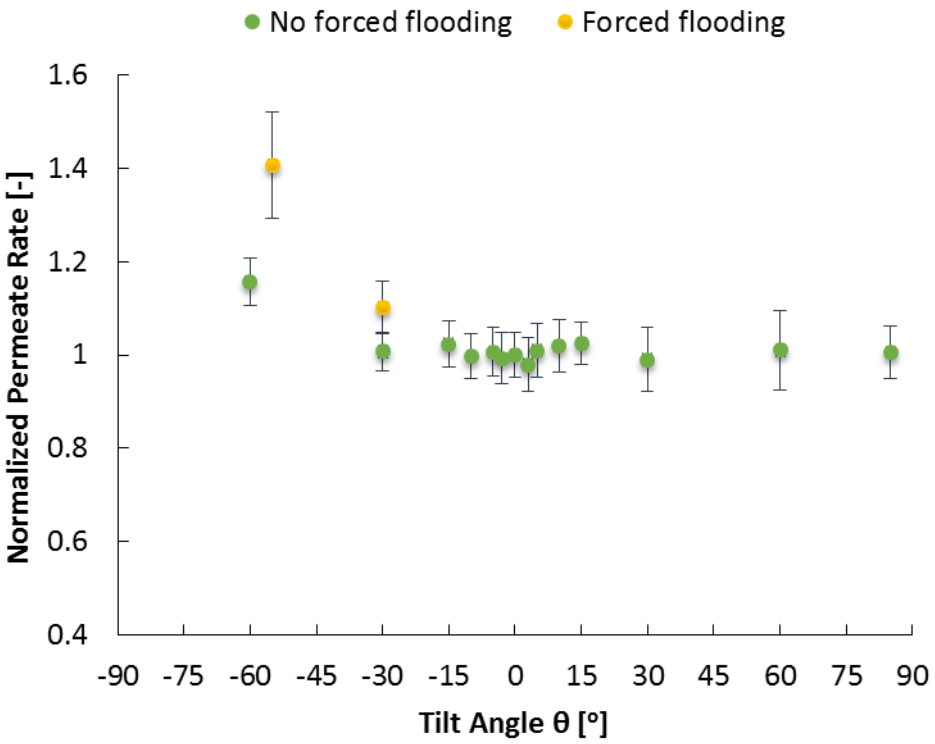

Figure 4-8: Effect of module tilt angle on permeate production: Comparison with modified experiment where hydrostatic forced flooding is avoided. $T_{\mathrm{f,in}} = 50\,^{\circ}\mathrm{C}$, $T_{\mathrm{c,in}} = 20\,^{\circ}\mathrm{C}$

permeate flux at small negative angles, indicating a lack of thermal bridging. The key insight is that thermal bridging is not a concern at vertical and near vertical angles for the air gap and spacer dimensions considered here.

An explanation for the why fluid does not fall onto the MD membrane even at negative inclinations may be obtained by the considering the hydrophobicity or hydrophilicity of the surface on which the fluid flows. The aluminum condensing surface is hydrophilic: typical aluminum condensing surfaces have contact angles around 5° [64]. Meanwhile, MD membranes are hydrophobic. Thin films of water can remain on the underside of inclined hydrophilic surfaces up to very high angles of inclination [65, 66, 67]. Additionally, in small gaps where droplets can easily exceed the size of the gap, droplets on the hydrophobic surface may touch and be reabsorbed into the film on the hydrophilic condensing plate. Therefore, large tilt angles, which favor thicker liquid films, may be required before thermal bridging effects occur.

4.6 Conclusions

The experimental and theoretical results indicate that moderate angles of inclination only had a minor effect on permeate flux, except at high angles where it was quite significant. Permeate flux varied by less than 5% within inclination angles of $\pm 15°$, but flux increased significantly as angles approached $\pm 90°$, in some cases rising by more than 40%.

The results indicate AGMDs susceptibility to two conditions in which liquid water spans the air gap, flooding and thermal bridging. Flooding, occurring when permeate production was rapid enough to fill the air gap with permeate, is a risk at large temperature differences across the air gap, at small gap sizes, and at very high inclined or declined angles. Flooding occurs primarily at very high inclined or declined angles.

The second condition, thermal bridging, occurs at high declined angles, for which condensate detaches from the laminar film on the condenser plate and makes contact with the hot membrane surface. This condition occurred more readily than flooding at declined angles, but was not observed for angles less than $30°$ off vertical. Results suggest that thermal bridging and flooding are likely to occur earlier, at smaller negative inclination angles, in systems that have lower air gap thickness.

While in many cases flooding and thermal bridging may reduce thermal efficiency, in single pass systems with limited size or lacking energy recovery, the increased permeate production from high incline angles with flooding or thermal bridging is often desirable, as more pure water is produced under the same cycle top and bottom temperature conditions.

Bibliography

[1] M. El-Bourawi, Z. Ding, R. Ma, and M. Khayet, "A framework for better understanding membrane distillation separation process," *Journal of Membrane Science*, vol. 285, pp. 4–29, Nov. 2006.

[2] E. K. Summers, H. A. Arafat, and J. H. Lienhard, "Energy efficiency comparison of single-stage membrane distillation (MD) desalination cycles in different configurations," *Desalination*, vol. 290, pp. 54–66, 2012.

[3] U. N. D. Program, "Human development report." `http://www.un.org/waterforlifedecade/scarcity.shtml,2006`.

[4] IDA, "Desalination yearbook, section 1. market profile." International Desalination Association, 2011 - 2012.

[5] K. H. Mistry, R. K. McGovern, G. P. Thiel, E. K. Summers, S. M. Zubair, and J. H. Lienhard V, "Entropy Generation Analysis of Desalination Technologies," *Entropy*, vol. 13, pp. 1829–1864, Sept. 2011.

[6] K. B. Gregory, R. D. Vidic, and D. A. Dzombak, "Water management challenges associated with the production of shale gas by hydraulic fracturing," *Elements*, vol. 7, no. 3, pp. 181–186, 2011.

[7] E. Curcio and E. Drioli, "Separation & Purification Reviews Membrane Distillation and Related Operations – A Review," *Separation and Purification Reviews*, vol. 34, pp. 35–86, 2005.

[8] A. S. Hassan and H. E. Fath, "Review and assessment of the newly developed MD for desalination processes," *Desalination and Water Treatment*, vol. 51, no. 1-3, pp. 574–585, 2013.

[9] S. Shirazi, C.-J. Lin, and D. Chen, "Inorganic fouling of pressure-driven membrane processes – A critical review," *Desalination*, vol. 250, no. 1, pp. 236–248, 2010.

[10] H. Susanto, "Towards practical implementations of membrane distillation," *Chemical Engineering and Processing: Process Intensification*, vol. 50, no. 2, pp. 139–150, 2011.

[11] M. Khayet, "Membranes and theoretical modeling of membrane distillation: a review," *Advances in colloid and interface science*, vol. 164, no. 1-2, pp. 56–88, 2011.

[12] Edited by Belmiloudi, Aziz, *Heat Transfer - Theoretical Analysis, Experimental Investigations and Industrial Systems*. InTech, 2011.

[13] K. Lawson and D. Lloyd, "Membrane distillation," *Journal of Membrane Science*, vol. 124, no. 1, pp. 1–25, 1997.

[14] A. Antony, J. H. Low, S. Gray, A. E. Childress, P. Le-Clech, and G. Leslie, "Scale formation and control in high pressure membrane water treatment systems: A review," *Journal of Membrane Science*, vol. 383, no. 1-2, pp. 1–16, 2011.

[15] R. B. Saffarini, E. K. Summers, H. A. Arafat, and J. H. Lienhard V, "Economic evaluation of stand-alone solar powered membrane distillation systems," *Desalination*, vol. 299, pp. 55–62, 2012.

[16] J. Koschikowski, M. Wieghaus, and M. Rommel, "Solar thermal-driven desalination plants based on membrane distillation," *Desalination*, vol. 156, no. 1-3, pp. 295–304, 2003.

[17] F. Banat, N. Jwaied, M. Rommel, J. Koschikowski, and M. Wieghaus, "Desalination by a "compact SMADES" autonomous solar powered membrane distillation unit," *Desalination*, vol. 217, no. 1-3, pp. 29–37, 2007.

[18] F. Banat, N. Jwaied, M. Rommel, J. Koschikowski, and M. Wieghaus, "Performance evaluation of the "large SMADES" autonomous desalination solar-driven membrane distillation plant in Aqaba, Jordan," *Desalination*, vol. 217, no. 1-3, pp. 17–28, 2007.

[19] E. Guillen-Burrieza, R. Thomas, B. Mansoor, D. Johnson, N. Hilal, and H. Arafat, "Effect of dry-out on the fouling of PVDF and PTFE membranes under conditions simulating intermittent seawater membrane distillation (SWMD)," *Journal of Membrane Science*, vol. 438, pp. 126–139, 2013.

[20] A. Alkhudhiri, N. Darwish, and N. Hilal, "Membrane distillation: A comprehensive review," *Desalination*, vol. 287, pp. 2–18, Feb. 2012.

[21] L. Martinez-Diez and M. Vazquez-Gonzalez, "Temperature and concentration polarization in membrane distillation of aqueous salt solutions," *Journal of Membrane Science*, vol. 156, no. 2, pp. 265 – 273, 1999.

[22] G. P. Narayan, M. H. Sharqawy, S. Lam, S. K. Das, and J. H. Lienhard V, "Bubble columns for condensation at high concentrations of non condensable gas: Heat transfer model and experiments," *AIChE Journal*, vol. 59, no. 5, pp. 1780–1790, 2012.

[23] S.A.Klein, "Engineering equation solver version 9." `http://www.fchart.com/ees/`.

[24] R. Hyland and A. Wexler, "Formulations for the thermodynamic properties of the saturated phases of H2O from 173.15K to 473.15K," *ASHRAE Transactions (Part 2A)*, 1983.

[25] A. Pruss and W. Wagner, "The IAPWS formulation 1995 for the thermodynamic properties of ordinary water substance for general and scientific use," *Journal of Physical and Chemical Reference Data*, vol. 2, pp. 387–535, 2002.

[26] M. Khayet, P. Godino, and J. I. Mengual, "Theory and experiments on sweeping gas membrane distillation," *Journal of Membrane Science*, vol. 165, no. July 1999, pp. 261–272, 2000.

[27] M. Khayet, M. P. Godino, and J. I. Mengual, "Thermal boundary layers in sweeping gas membrane distillation processes," *AIChE Journal*, vol. 48, pp. 1488–1497, July 2002.

[28] K. Charfi, M. Khayet, and M. Safi, "Numerical simulation and experimental studies on heat and mass transfer using sweeping gas membrane distillation," *Desalination*, vol. 259, pp. 84–96, Sept. 2010.

[29] J. Swaminathan and J. H. Lienhard V, "Energy efficiency of Sweeping Gas Membrane Distillation cycles," in *Proceedings of the 11th ISHMT-ASME Heat and Mass Transfer Conf., Kharagpur*, ISHMT-ASME, 2013.

[30] J. H. Lienhard V and J. H. Lienhard IV, *A Heat Transfer Textbook, Fourth Edition*. Dover Publications, Inc., 2011.

[31] E. W. Tow and J. H. Lienhard V, "Heat Flux and Effectiveness in Bubble Column Dehumidifiers," in *Proceedings of the 2013 IDA World Congress on Desalination and Water Reuse*, IDA, 2013.

[32] G. P. Narayan, J. H. Lienhard V, and S. M. Zubair, "Entropy generation minimization of combined heat and mass transfer devices," *International Journal of Thermal Sciences*, vol. 49, no. 10, pp. 2057 – 2066, 2010.

[33] C. Cabassud and D. Wirth, "Membrane distillation for water desalination: How to choose an appropriate membrane?," *Desalination*, vol. 157, no. 1-3, pp. 307–314, 2003.

[34] D. L. Shaffer, L. H. Arias Chavez, M. Ben-Sasson, S. Romero-Vargas Castrillon, N. Y. Yip, and M. Elimelech, "Desalination and reuse of high-salinity shale gas produced water: drivers, technologies, and future directions," *Environmental science & technology*, vol. 47, no. 17, pp. 9569–9583, 2013.

[35] M. Khayet and T. Matsuura, *Membrane Distillation Principles and Applications*. Elsevier, 2011.

[36] N. Epstein, "Thinking about heat transfer fouling: A 5 5 matrix," *Heat Transfer Engineering*, vol. 4, no. 1, pp. 43–56, 1983.

[37] T. Y. Cath, V. Adams, and A. E. Childress, "Experimental study of desalination using direct contact membrane distillation: a new approach to flux enhancement," *Journal of Membrane Science*, vol. 228, no. 1, pp. 5 – 16, 2004.

[38] E. K. Summers, *Energy Efficiency of membrane distillation*. PhD thesis, Massachusetts Institute of Technology, 2013.

[39] McMaster-Carr, "Viton Fluoroelastomer O-Ring Cord Stock , Part Number 96515K42." http://www.mcmaster.com/?error_redirect=true#96515k42/=rrt8jz.

[40] R. D. Blevins, *Applied Fluid Dynamics Handbook*. Krieger Publishing, 2003.

[41] Millipore, "Immobilon-PSQ Membrane, PVDF, Part Number ISEQ00010." http://www.millipore.com/catalogue/item/ISEQ00010.

[42] Cole-Parmer, "Magnetic Drive PP Centrifugal Pump with Enclosed Motor; 18.4 GPM/26.9 ft, 115V, Part Number 72010-60." http://www.coleparmer.com/Product/Mag_Drive_PP_Centrifugal_Pump_w_Enclosed_Motor_18_4_GPM_26_9_ft_115V/EW-72010-60.

[43] Cole-Parmer, "Magnetic Drive PP Centrifugal Pump with Enclosed Motor; 8.2 GPM/14.1 ft, 115V, Part Number 72010-30." http://www.coleparmer.com/Product/Mag_Drive_PP_Centrifugal_Pump_w_Enclosed_Motor_8_2_GPM_14_1_ft_115V/EW-72010-30.

[44] Omega, "Pipe-Plug Thermistor Probes, Part Number TH-44004-1/4NPT-80." http://www.omega.com/pptst/TH-44000-NPT.html.

[45] Cole-Parmer, "Cole-Parmer multi-sensor temperature logger w/onboard memory card, Part Number USB-5203." http://www.coleparmer.com/buy/product/68114-cole-parmer-multi-sensor-temperature-logger-w-onboard-memory-card.html.

[46] McMaster-Carr, "Splash-Resistant Water Flowmeter, 1/2 Pipe, Part Number 3562K12." http://www.mcmaster.com/#3562k12/=rrshfc.

[47] McMaster-Carr, "Splash-Resistant Water Flowmeter, 3/8 Pipe, Part Number 3562K11." http://www.mcmaster.com/#3562k11/=rrsi3p.

[48] McMaster-Carr, "Digital Bench Scale with Stainless Steel Platform 70.55 oz/ 2000 G Capacity, Part Number 1760T86." http://www.mcmaster.com/#1760t86/=rrt04f.

[49] K. Scientific, "Jenco 3250 portable Conductivity meter." http://www.katsci.com/products/jenco-3250-portable-meter.aspx.

[50] A. L. Zydney, "Stagnant film model for concentration polarization in membrane systems," *Journal of Membrane Science*, vol. 130, no. 1, pp. 275–281, 1997.

[51] S. Bhattacharjee, J. C. Chen, and M. Elimelech, "Coupled model of concentration polarization and pore transport in crossflow nanofiltration," *AIChE journal*, vol. 47, no. 12, pp. 2733–2745, 2001.

[52] K. H. Mistry and J. H. Lienhard, "Effect of nonideal solution behavior on desalination of a sodium chloride (NaCl) solution and comparison to seawater," in *ASME 2012 International Mechanical Engineering Congress and Exposition*, pp. 1509–1523, American Society of Mechanical Engineers, 2012.

[53] R. A. Robinson and R. H. Stokes, *Electrolyte solutions*. Courier Dover Publications, 2002.

[54] E. K. Summers and J. H. Lienhard V, "A novel solar-driven air gap membrane distillation system," *Desalination and Water Treatment*, vol. 51, pp. 1–8, 2012.

[55] J. Gilron, L. Song, and K. K. Sirkar, "Design for Cascade of Crossflow Direct Contact Membrane Distillation," *Industrial & Engineering Chemistry Research*, vol. 46, no. 8, pp. 2324–2334, 2007.

[56] F. He, J. Gilron, and K. K. Sirkar, "High water recovery in direct contact membrane distillation using a series of cascades," *Desalination*, vol. 323, pp. 48–54, 2013.

[57] G. Zaragoza, A. Ruiz-Aguirre, E. Guillen-Burrieze, D. Alarcon-Padilla, and J. Blanco-Galvez, "Experimental comparison of different prototypes of solar energy driven membrane distillation systems," in *Proceedings of the 2013 IDA World Congress on Desalination and Water Reuse*, 2013.

[58] K. Zhao, W. Heinzl, M. Wenzel, S. Büttner, F. Bollen, G. Lange, S. Heinzl, and N. Sarda, "Experimental study of the memsys vacuum-multi-effect-membrane-distillation (V-MEMD) module," *Desalination*, vol. 323, pp. 150–160, 2013.

[59] G. L. Liu, C. Zhu, C. S. Cheung, and C. W. Leung, "Theoretical and experimental studies on air gap membrane distillation," *Heat and Mass Transfer*, vol. 34, no. 4, pp. 329–335, 1998.

[60] A. Alkhudhiri, N. Darwish, and N. Hilal, "Produced water treatment: Application of air gap membrane distillation," *Desalination*, pp. 46–51, 2013.

[61] G. Chen, X. Yang, R. Wang, and A. G. Fane, "Performance enhancement and scaling control with gas bubbling in direct contact membrane distillation," *Desalination*, vol. 308, pp. 47–55, 2013.

[62] D. E. M. Warsinger, J. Swaminathan, and J. H. Lienhard V, "Effect of module inclination angle on Air Gap Membrane Distillation," in *Proceedings of the 15th International Heat Transfer Conference*, IHTC, 2014.

[63] A. Mills, *Heat Transfer 2nd Edition*. Prentice Hall, 1998.

[64] J. Bernardin, I. Mudawar, C. Walsh, and E. Franses, "Contact angle temperature dependence for water droplets on practical aluminum surfaces," *International Journal of Heat and Mass Transfer*, vol. 40, no. 5, pp. 1017–1033, 1997.

[65] H. R. Nagendra, "Effect of inclination on laminar film condensation," *Applied Scientific Research*, vol. 28, pp. 261–277, 1973.

[66] J. A. Howarth, G. Poots, and D. Wynne, "Laminar film condensation on the underside of an inclined flat plate," *Mechanics Research Communications*, vol. 5, no. 6, pp. 369–374, 1978.

[67] B. J. Chung and S. Kim, "Film condensations on horizontal and slightly inclined upward and downward facing plates," *Heat Transfer Engineering*, vol. 29, pp. 936–941, 2008.